CHARACTERIZATION AND OPTIMIZATION OF AN X-RAY LASER FOR THE SPECTROSCOPY OF LI-LIKE HEAVY-IONS

DISSERTATION
ZUR ERLANGUNG DES GRADES
"DOKTOR DER NATURWISSENSCHAFTEN"
AM FACHBEREICH PHYSIK, MATHEMATIK UND INFORMATIK
DER JOHANNES GUTENBERG-UNIVERSITÄT
IN MAINZ

Bernhard Zielbauer
geb. in Heidelberg
Mainz, den 24.10.2007

D77 (Dissertation Universität Mainz)

ABSTRACT

Recent developments in the theory of plasma-based collisionally excited x-ray lasers (XRL) have shown an optimization potential based on the dependence of the absorption region of the pumping laser on its angle of incidence on the plasma. For the experimental proof of this idea, a number of diagnostic schemes were developed, tested, qualified and applied. A high-resolution imaging system, yielding the keV emission profile perpendicular to the target surface, provided positions of the hottest plasma regions, interesting for the benchmarking of plasma simulation codes. The implementation of a highly efficient spectrometer for the plasma emission made it possible to gain information about the abundance of the ionization states necessary for the laser action in the plasma. The intensity distribution and deflection angle of the pump laser beam could be imaged for single XRL shots, giving access to its refraction process within the plasma. During a European collaboration campaign at the Lund Laser Center, Sweden, the optimization of the pumping laser incidence angle resulted in a reduction of the required pumping energy for a Ni-like Mo XRL, which enabled the operation at a repetition rate of 10 Hz. Using the experiences gained there, the XRL performance at the PHELIX facility, GSI Darmstadt with respect to achievable repetition rate and at wavelengths below 20 nm was significantly improved, and also important information for the development towards multi-100 eV plasma XRLs was acquired. Due to the setup improvements achieved during the work for this thesis, the PHELIX XRL system now has reached a degree of reproducibility and versatility which is sufficient for demanding applications like the XRL spectroscopy of heavy ions. In addition, a European research campaign, aiming towards plasma XRLs approaching the water-window (wavelengths below 5 nm) was initiated.

ZUSAMMENFASSUNG

Neue Entwicklungen auf dem Gebiet der Theorie der plasmabasierten, Elektronenstoß-angeregten Röntgenlaser (XRL) haben ein Optimierungspotential aufgezeigt, das auf der Abhängigkeit des Absorptionsbereichs des Pumplasers von seinem Auftreffwinkel auf das Plasma beruht. Für eine experimentelle Verifizierung dieses Ansatzes wurden im Laufe dieser Arbeit mehrere Diagnostiken entwickelt sowie getestet, charakterisiert und eingesetzt. Ein hochauflösendes Abbildungssystem, das Emissions-Profile im keV-Bereich senkrecht zur Targetoberfläche lieferte, ermöglichte die Bestimmung der Positionen der heißesten Plasmabereiche, welche für die Bewertung und Verifizierung von Plasma-Simulations-Codes

interessant sind. Die Intensitätsverteilung und der Ablenkungswinkel des Pumplaser-Strahls konnten für einzelne Röntgenlaser-Schüsse ermittelt werden, was Zugang zum Beugungsprozeß innerhalb des Plasmas gewährt. Während einer Strahlzeit im Rahmen einer europäischen Kollaboration am Lund Laser Center in Schweden gelang es durch die Optimierung des Pumplaser-Auftreffwinkels, die Reduktion der benötigten Pumpenergie für einen Ni-ähnlichen Mo XRL auszunutzen, um den Betrieb bei 10 Hz Repetitionsrate zu ermöglichen. Die Verwendung der hier gewonnenen Erfahrungen erlaubte es, die Leistungsfähigkeit des Röntgenlasers des PHELIX-Systems an der GSI Darmstadt auch bei Wellenlängen wesentlich unterhalb von 20 nm bezüglich der erreichbaren Schußrate zu steigern. Des weiteren ergaben sich wichtige Hinweise für Entwicklungen von XRLs in den Röntgenbereich von mehreren 100 eV. Aufgrund der Weiterentwicklung des Aufbaus, die während der Durchführung dieser Arbeit erreicht wurde, hat das PHELIX-Röntgenlasersystem einen Grad an Reproduzierbarkeit und Vielseitigkeit erreicht, der nun den Einsatz in anspruchsvollen Anwendungen wie der Röntgenlaser-Spektroskopie an schweren Ionen ermöglicht. Zudem wurde eine europäische Experimentierkampagne initiiert, die das Erreichen des Wasser-Fensters bei Wellenlängen unterhalb von 5 nm zum Ziel hat.

CONTENTS

1 INTRODUCTION

Since the first experimental demonstration in the mid-1980s, the term "x-ray laser" has been employed by a growing community of researchers in this field to denominate quasi-monochromatic, partially coherent light sources with wavelengths shorter than a few tens of nanometers. To begin with, an overview of different types of existing sources of radiation in this regime is given, out of which the work at hand will focus then on the plasma-based x-ray lasers, concluding the introduction with a short summary of their development history.

1.1 PRESENTLY AVAILABLE SOURCES FOR XUV RADIATION

SYNCHROTRON RADIATION Originating from the centripetal acceleration of relativistic electrons (or positrons), a wide spectrum from the infrared up to hard x-rays can be covered. Since the discovery of the effect in 1947, continuous development has made dedicated synchrotron facilities very attractive light sources, mostly because of their wide tunability and high intensity. Meanwhile, the so-called third-generation sources, employing special magnetic structures (wigglers, undulators) with photon energies of up to 8 GeV (SPring-8, Japan), are able to exceed a spectral brightness of 10^{20} photons/s/mm^2/mrad^2/0.1% BW, where 0.1% BW denotes a bandwidth of $10^{-3} \times \omega$ centered around the frequency ω.

FREE ELECTRON LASERS (FEL) In addition to the acceleration of electrons, FELs employ the principle of self-amplified spontaneous emission (SASE). An electron beam guided through an undulator with a cycle length of λ_u will produce an incoherent radiation field with the wavelength

$$\lambda = \frac{\lambda_u}{2\gamma^2}, \tag{1.1}$$

where $\gamma = E_e/mc^2$ is the electrons' relativistic factor for a given electron energy E_e. The emitted radiation can interact again with the electron beam, leading to a self-amplified modulation of the electron density, causing more and more electrons to emit in phase until the onset of saturation effects. In difference to the case of synchrotron radiation which scales linearly with the number of electrons, the coherent FEL emission scales quadratically, which gives a strong boost to the achievable photon flux. One of the most advanced facilities is the FLASH facility at DESY,

Hamburg, Germany, currently delivering a peak spectral brightness of 6×10^{29} photons/s/mm^2/mrad^2/0.1 % BW [1].

INCOHERENT PLASMA EMISSION The emission of hot plasmas can be estimated from its black body radiation via Wien's law

$$\lambda_{max} = \frac{2.8978 \times 10^{-3}\,\mathrm{m \cdot K}}{T}. \tag{1.2}$$

For example, for the emission maximum to be at 20 nm, the plasma temperature has to be roughly 145000 K (or 12.5 eV), which can be reached by high electrical currents ("pinches") or laser excitation. Depending on the electronic structure of the ions in the plasma, the emission spectrum can either be quasi-continuous (e.g., xenon, metals) or dominated by lines (e.g., light gases), where line widths of $\Delta\lambda/\lambda = 5 \times 10^{-4}$ have been measured [2]. Due to their compact and robust design, plasma sources are expected to be the most promising choice as light sources for EUV lithography (see, e.g., [3]) in the semiconductor industry's unbroken strive for smaller structures.

HIGH HARMONIC GENERATION (HHG) By focusing a linearly polarized, high-intensity short-pulse laser into a gas target, odd multiples ("harmonics") of the laser frequency can be obtained due to nonlinear interaction with the gas atoms. A simplified explanation of this effect is based on the approach that in the strong, slowly varying field of the laser, the Coulomb field of the atoms is deformed to a degree where ionization via tunneling becomes possible. The electric laser field will accelerate a freed electron away from the nucleus until, after half an optical cycle, the field direction is reversed and the electron is accelerated back towards the atom. During the recombination with the atom, radiation is emitted, whose photons, due to the quasi-periodic nature of the effect, interfere to the characteristic comb-like frequency structure of odd integer multiples.

The advancement of ultrahigh-intensity lasers has lead to a continuous increase in the achieved harmonic number which lately allowed to exceed a photon energy of 1 keV [4]. Also the conversion efficiencies have improved tremendously and can nowadays be as high as 10^{-5} [5], although these values are only reached with very short and consequently broad-band lasers which results in similarly short and thus broadband harmonic pulses, limiting their use as direct sources for high-resolution spectroscopy. However, their high beam quality and spatial coherence makes them ideal as seed laser sources which can be amplified by plasma-based approaches, combining the HHG beam qualities with the high gain of plasma-based lasers.

PLASMA-BASED X-RAY LASERS (XRL) As will be shown in more detail in chapter 2, the creation and heating process of a laser-produced

plasma can be optimized to form an amplification medium similar to classical gas lasers, but with higher densities and shorter transition wavelengths. Mostly due to the short lifetime of the population inversion, the use of cavities with several passes through the medium is not possible (although half-cavities have been demonstrated [6] [7]), so most schemes so far have been based on the amplification of spontaneous emission. Still, with the high densities and high gain coefficients, even several millimeters of plasma column length can produce strongly peaked emission, depending in wavelength on the transitions of the involved ion species, i.e., the employed target material. Peak spectral brightnesses of up to 10^{28} photons/s/mm^2/mrad^2/0.1 % BW have been demonstrated (also in the experiment described in chapter 4.1.1), making them a competition to the FELs mentioned above without the need for a linear accelerator.

1.2 SHORT HISTORY OF XRL DEVELOPMENT

The first collisionally pumped XRL was demonstrated at LLNL, USA in 1984 [8], using a pumping laser energy of typically 500 J and thin lasing material layers deposited on foils. Subsequently, the required pumping energy was significantly reduced by using more massive slab targets instead of foils [9], and by the transition to multiple-pulse pumping around 1994 [10] [11], the latter helping to establish low plasma gradients by introducing an expansion phase between the pulses. This was improved further by the use of a short (CPA) pulse to heat the plasma, clearly separating the plasma production from the heating phase needed for the inversion [12], the so-called transient excitation scheme. Traveling wave pumping (see chapter 2.5.1) had to be introduced to match the position of the short-lived gain with the transit of the generated XRL pulse, which was further refined by introducing longer delays between the prepulse and the main pulse [13].

The up to date last major advance became possible with the scheme of grazing incidence pumping (GRIP, see chapter 2.5.2) which enabled the deposition of the main pulse energy in the anticipated region of gain by bringing the main pulse onto the target under a near-grazing angle. First experiments using such a scheme were published by the GSI-MBI-LIXAM collaboration in 2002 [14] [15] [16]. Gain at wavelengths as low as 10 nm has been observed using this scheme with pump energies around 1 J [17] [18]. With these parameters and an improved stability of the laser output due to refinements of the pumping geometry, plasma XRLs are on the way to become a versatile and useful tool for XUV experiments. The advancements presented in this work represent part of this developmental path.

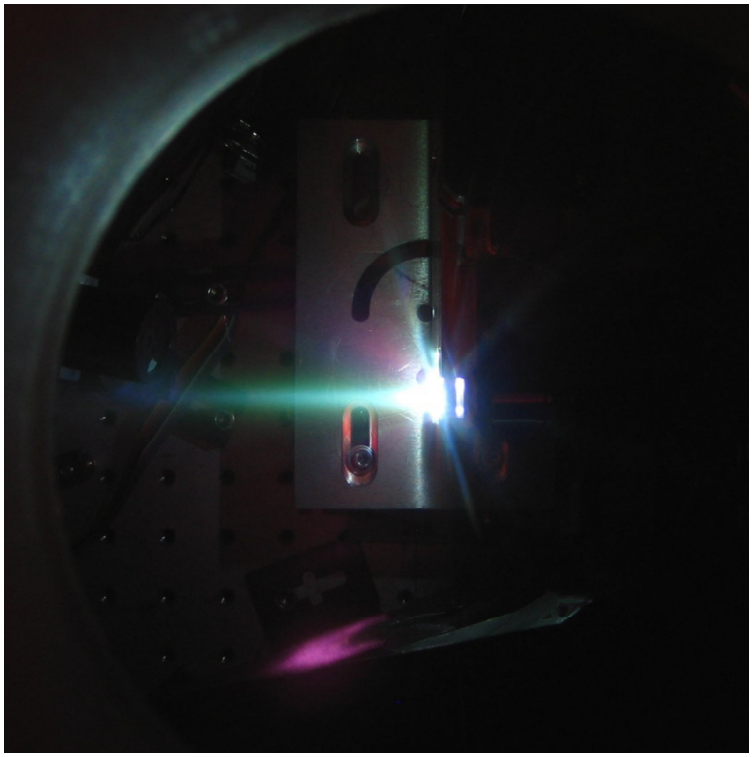

Figure 1: Photograph of a typical Pd XRL shot seen through a window directly above the target. The green plasma plume expanding towards the uncompressed pulse (see chapter 2.5) coming from the left side is clearly visible. In the lower part, also the sickle-shaped image of the refracted main pulse (see chapter 4.2.6) can be seen.

2 BASICS OF XRL OPERATION

2.1 PLASMA GENERATION WITH INTENSE LASERS

As long as the photon energy of an incoming high-intensity laser pulse is lower than the work function of the target material, the most effective way a solid target can absorb the pulse's energy is via multiphoton ionization. The resulting free electrons are then accelerated in the laser's oscillating electric field via the so-called inverse bremsstrahlung effect, and those hitting the target surface again will cause further ionization, heating and ablation of target material. After a few hundreds of femtoseconds, a plasma cloud, consisting of ions and hot electrons, will expand away from the target surface, producing a density gradient which is decaying exponentially with the distance to the target. The plasma can be characterized by the oscillation frequency of the movement the electrons perform with respect to the ions, the plasma frequency

$$\omega_P = \sqrt{\frac{N_e e^2}{m_e \epsilon_0}} \tag{2.1}$$

for a given electron density N_e. Equating this with the laser frequency $\omega_L = 2\pi c/\lambda$ leads to the critical electron density [19]

$$N_c = \frac{m_e \epsilon_0}{e^2} \left(\frac{2\pi c}{\lambda} \right)^2 , \tag{2.2}$$

depending only on physical constants and the laser wavelength (see also figure 2).

At this density, the plasma will effectively shield the target from direct laser light by either reflection or resonance absorption. In the region of higher ("overcritical") density, further heating is effected via the hot electrons, while the undercritical part can be heated more by inverse bremsstrahlung.

2.2 PLASMA DYNAMICS

The interactions between the electrons, ions and atoms in a plasma can be divided into collisional and radiative effects, namely collisional excitation, deexicitation and ionization and three-body recombination on one hand, and radiative excitation, deexicitation and recombination, photo and autoionization and dielectronic recombination on the other.

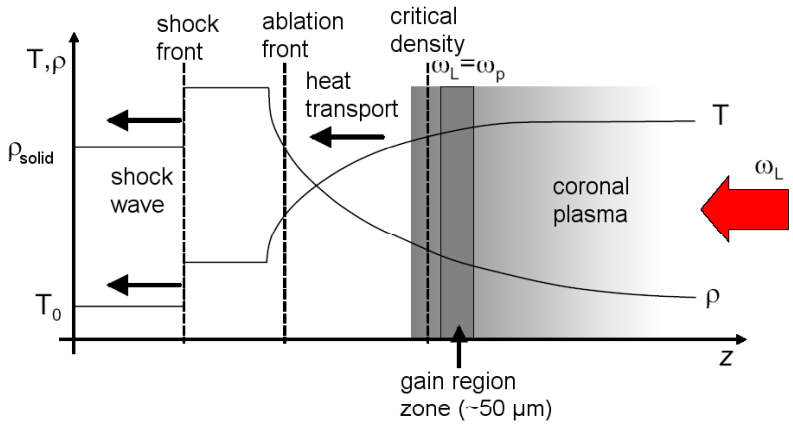

Figure 2: Temperature and density distributions in a laser-produced plasma [20].

On time and distance scales which are small compared to the plasma development dimensions, a local thermal equilibrium (LTE) can form in a plasma parameter regime where the collisional processes dominate the radiative ones. This is fulfilled in weakly ionized high-density plasmas which is expressed in criteria like [21]

$$N_e \geq 1.9 \times 10^{16} [\mathrm{cm}^{-3}] \frac{E_{ik}}{[\mathrm{eV}]} \sqrt{\frac{T_e}{[\mathrm{eV}]}}, \tag{2.3}$$

for a given electron temperature T_e, favoring conditions with small energy differences E_{ik} between different levels i and k. Here, the collisional excitation and ionization are balanced by their inverse processes, resulting in a Boltzmann distribution for the population ratio of bound states within one ionization state:

$$\frac{N_k}{N_i} = \frac{g_k}{g_i} e^{-\frac{E_{ik}}{k_B T_e}}, \tag{2.4}$$

where g_x denotes the respective degeneracy. The population ratio of bound states of adjacent ionization states Z and $Z+1$ can be described by the Saha equation [22]

$$\frac{N_k^{Z+1}}{N_i^Z} = \frac{g_k^{Z+1}}{g_i^Z} \left(\frac{1}{N_e} \frac{2}{a_0^3} \left(\frac{kT_e}{4\pi E_H} \right)^{3/2} \right) \exp\left(-\frac{E_{ik}}{k_B T_e} \right), \tag{2.5}$$

where a_0 is the Bohr radius and E_H is the ionization energy of hydrogen.

In plasmas with lower densities and higher ionization states (resulting in higher E_{ik} values), the radiative processes dominate. However, for optically thin plasmas where the emitted radiation is not absorbed by the

plasma, the deexcitation is radiative while the excitation happens mostly by collisional processes, resulting in a so-called coronal equilibrium. Typical x-ray laser plasmas show properties of both cases and thus must be described by a collisional-radiative model [23]. As will be shown in chapter 2.3, the upper x-ray laser level is energetically close to the adjacent levels, so it has to be treated within the LTE model, while the energy difference between the lower x-ray laser level and the ground state is bigger which means that it is depopulated mainly by radiative processes.

2.3 LASER GAIN IN PLASMAS

The x-ray laser scheme described here is based on the amplification of spontaneous emission ("ASE"), so a short outline of the underlying physical context will be given. An excited atom or ion in the energy state E_u can transit to the lower state E_l via the emission of a photon in two distinctly different ways. Without the influence of an external electromagnetic field, this transition happens via spontaneous emission, resulting in a photon with the energy $h\nu = E_u - E_l$ with an arbitrary combination of direction, phase and polarization. The rate of spontaneous transition A_{ul} is the inverse of the natural lifetime of the $u \rightarrow l$ transition. For a given number N_u of excited atoms or ions in the state u, the temporal change of the population is given by

$$-\left(\frac{\mathrm{d}N_u}{\mathrm{d}t}\right)_{sp} = A_{ul}N_u. \tag{2.6}$$

An external electromagnetic field with the frequency $\nu = \frac{E_u - E_l}{h}$ can open the possibility of a transition by stimulated emission, induced by a photon from the external field. This produces a photon with identical properties due to the fact that it is emitted into the same phase space cell. The stimulated emission rate is proportional to the spectral energy density ρ_ν of the radiation field, reduced by the transition bandwidth $\Delta\nu$ in the case of a monochromatic field:

$$\left(\frac{\mathrm{d}N_u}{\mathrm{d}t}\right)_{st} = \frac{B_{ul}\rho_\nu}{\Delta\nu}. \tag{2.7}$$

The coefficients A and B are named after A. Einstein who deduced the well-known relation [24]

$$\frac{A_{ul}}{B_{ul}} = \frac{8\pi h}{\lambda^3}. \tag{2.8}$$

The time-reversed process of a stimulated $u \rightarrow l$ emission is the absorption of a photon resulting in a transition from state l to the energetically

higher state u and has the same transition rates, corrected for their respective degeneracies g_l and g_u:

$$\frac{B_{ul}}{g_l} = \frac{B_{lu}}{g_u}. \tag{2.9}$$

Neglecting the spontaneous emission, the temporal change of spectral energy density at the frequency ν and a transition bandwidth $\Delta\nu$ thus can be written as

$$\frac{\mathrm{d}\rho_\nu}{\mathrm{d}t} = (B_{ul}N_u - B_{lu}N_l)\frac{\rho_\nu}{\Delta\nu}. \tag{2.10}$$

With $\frac{\mathrm{d}\rho_\nu}{\mathrm{d}t} = \frac{1}{c}\frac{\mathrm{d}I_\nu}{\mathrm{d}t} = \frac{\mathrm{d}I_\nu}{\mathrm{d}z}$ and equations 2.8 and 2.9, the differential equation for the intensity increment per path length $\mathrm{d}z$ is given by

$$\frac{\mathrm{d}I_\nu}{\mathrm{d}z} = \left(N_u - \frac{g_u}{g_l}N_l\right)\frac{A_{ul}\lambda^3}{8\pi\Delta\nu}I_\nu = gI_\nu \tag{2.11}$$

with a solution in the form of

$$I_\nu(l) = I_\nu(0)\exp(gl), \tag{2.12}$$

where

$$g = \frac{A_{ul}\lambda^3}{8\pi\Delta\nu}\left(N_u - \frac{g_u}{g_l}N_l\right) = \sigma_{\mathrm{stim}}\left(N_u - \frac{g_u}{g_l}N_l\right). \tag{2.13}$$

The gain coefficient g [cm^{-1}] is dependent on the absorption cross section

$$\sigma_{\mathrm{stim}} = \frac{A_{ul}\lambda^3}{8\pi\Delta\nu} \tag{2.14}$$

and the population of the considered states, which in thermal equilibrium results in $g < 0$ and the exponential attenuation of an incident light field. So, in order to achieve an amplification of the incident light field, a population inversion ($N_l \ll N_u$) is necessary, requiring a pumping power $P_p \propto g/\lambda^4$ [25] which explains the need for high-power pumping laser systems for the realization of short-wavelength lasers.

Although at least the double-pass amplification in a plasma using an x-ray multilayer mirror [6] [7] has been demonstrated, most plasma-based (non seeded) x-ray lasers are working with the amplification of spontaneous emission (ASE). This is due to the fact that the lifetime of the population inversion is in the range of 1 ns which is not long enough to allow for several passes through the gain medium. In fact, in the excitation scheme on which the x-ray lasers presented here are based (see chapter 2.5), the gain lifetime is so short that one has to employ special techniques (see next paragraph) to make it last long enough for a single

pass through the plasma. Resultingly, the intensity to be amplified is not a quantity given from outside as assumed in eq. 2.13, but moreover the entire spontaneous emission along the length of the amplifying medium. Writing the spontaneous emission as

$$j(\nu) = N_u h\nu A_{ul}, \tag{2.15}$$

the radiation transport equation 2.11 becomes

$$\frac{dI_\nu}{dz} = g(\nu) I_\nu + j(\nu) \tag{2.16}$$

and the integration over the entire medium length l gives the overall intensity

$$I_\nu = \frac{j(\nu)}{g(\nu)} \left(\exp(g(\nu)l) - 1\right). \tag{2.17}$$

The so-called "gain-length" product gl is often treated as a measure for the achieved amplification.

It is possible to deduce the gain coefficient g from the intensity rise with increasing medium length l by fitting the experimental data with a model based on the so-called Linford formula [26]

$$I = \frac{\epsilon}{g} \frac{(\exp(gl) - 1)^{3/2}}{(gl \exp(gl))^{1/2}}, \tag{2.18}$$

which is an analytical approximation of the integral of eq. 2.17 over the frequency, taking into account the frequency dependence of the spontaneous emission and the amplification via appropriate line profile functions. A typical result of such a fit is shown in figure 33, clearly showing the transition between the small signal gain and the saturated gain regime [27].

The saturation is caused by the fact that a high rate of stimulated emission (contradicting the assumption of the deduction above) significantly reduces the population inversion. This is the case when the intensity is so high that the stimulated emission becomes comparable to the total rates of other processes depleting the upper laser level:

$$\frac{I}{h\nu}\sigma \approx r A_{ul}. \tag{2.19}$$

The value of $r > 1$ is taking into account radiational and collisional processes in addition to the spontaneous emission and can be determined from the level structure of the involved ions, the transition rates and cross sections as well as the density and temperature of the plasma, leading typically to values around $r \approx 10$. Together with eq. 2.14, the saturation

intensity can be estimated to

$$I_{\mathrm{sat}} = \frac{h\nu r A_{ul}}{\sigma} = \frac{8\pi h c^2 r \Delta\lambda/\lambda}{\lambda^4} \tag{2.20}$$

(see also, e.g., [28]). Reaching the regime of saturation is of importance since it makes efficient use of the energy stored in the population inversion and furthermore reduces the shot-to-shot variations due to the intensity dependent attenuation.

2.4 LASER PROPAGATION IN PLASMAS

The approach to make use of the strong intensity increase with higher values for the gain-length product by using longer and longer targets is limited by the refraction in the plasma caused by the electron density gradient, bending the trajectory of the XRL pulse out of the gain zone. The index of refraction n at position r caused by the electron density $N_e(r)$ is given by

$$n(r) = \sqrt{1 - \frac{N_{\mathrm{e}}(r)}{N_{\mathrm{c}}}} \approx 1 - \frac{N_{\mathrm{e}}(r)}{2N_{\mathrm{c}}}, \tag{2.21}$$

assuming $N_{\mathrm{e}} \ll N_{\mathrm{c}}$ which is true in the vicinity of the gain zone in typical x-ray lasers. Defining s as distance along the path of the XRL pulse and $\vec{r}$ as a position vector, Fermat's principle leads to the equation for a ray path [29]

$$\frac{\mathrm{d}}{\mathrm{d}s}\left(n\frac{\mathrm{d}\vec{r}}{\mathrm{d}s}\right) = \nabla n. \tag{2.22}$$

Assuming a medium with a refractive index close to unity and paraxial propagation along the z axis, it follows that

$$\frac{\mathrm{d}r^2}{\mathrm{d}z^2} = \frac{\mathrm{d}n}{\mathrm{d}x} = -\frac{1}{2N_{\mathrm{c}}} \cdot \frac{\mathrm{d}N_{\mathrm{e}}(x)}{\mathrm{d}x}. \tag{2.23}$$

This result can be generalized [30] to show that the trajectory of a ray in the plasma can be treated analog to the motion of a single particle in a potential with the same spatial variation as the electron density. Many ray tracing models (see, e.g., [31]) for the simulation of XRL are based on this idea and have lead to a better understanding of the XRL processes. For example, the implementation of a prepulse, forming a plasma which is given some time to expand before the arrival of the main pumping pulse, became rather obvious since this lowers the density gradients significantly, allowing the XRL pulse to propagate longer in the gain region. Also the idea of using targets bent in a curvature which matches the ray trajectory (originally proposed in [32]) follows this idea,

as do the approaches following an injector-amplifier design [33] [34].

2.5 TRANSIENT COLLISIONAL EXCITATION

Many pumping schemes to achieve the population inversion necessary for the lasing action have been proposed and many have also been demonstrated successfully (overviews can be found, e.g., in [35] or [36]). The following description is limited to the electron-collisional excitation scheme.

Neon-like ($Z - 10$) and nickel-like ($Z - 28$) ions are attractive candidates as lasing centers due to their closed shells and hence comparatively high energies needed to ionize them further, which makes them stable over a wide range of electron temperatures and densities. This scheme was proposed in the 1970s [37] [38], but the experimental demonstration followed not until 1985 [8] with a neon-like selenium laser at 20.63 and 20.96 nm. Figure 3 shows the energy level diagrams for the two ionization states with their respective lasing transitions, namely $3p \rightarrow 3s$ and $4d \rightarrow 4p$.

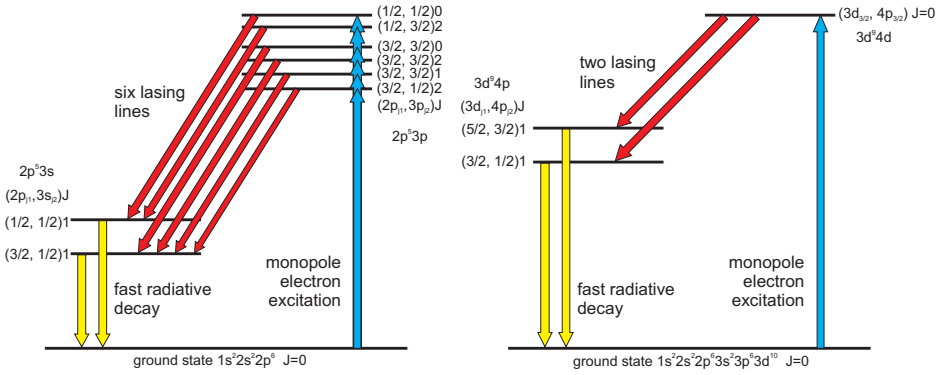

Figure 3: Schematic energy level diagram for the (a) neon-like and (b) nickel-like XRL (after [27]).

The upper laser levels are populated by monopole collisional excitation (the radiative dipole transitions are forbidden) and are metastable towards the ground states since radiative decay is forbidden for that case, while the lower laser level is depopulated rapidly by radiative dipole decay, resulting in the desired population inversion. X-ray lasers based on the scheme of electron collisional excitation have been demonstrated for many materials, ranging from neon-like argon ($\lambda = 46$ nm) to nickel-like gold ($\lambda = 3.7$ nm) [35]. The creation and heating of the plasmas is achieved mostly by using high energy, high power lasers which, due to the necessary plasma temperatures of (depending on the target material) more than 1 keV required pump laser intensities of up to 10^{14} W/cm^2. Laser pulse durations in the order of a nanosecond meant that the pulse

energies had to be at least several hundred Joule which limited research in this field to a few powerful laser systems.

A major step towards the reduction of the required pump laser energy was achieved with the transition from the quasi-steady-state (QSS) excitation to the transient excitation scheme [39] which was first demonstrated in 1997 [12]. The idea is to reach the necessary rate of excitation so fast that the time before the formation of a new ionization equilibrium is sufficient for a usable gain process which is then ended by the overionization of the ion species. The electron collisional excitation rate for a transition with energy ΔE

$$\langle \sigma v \rangle \propto \frac{N_e}{\sqrt{kT}} e^{-\frac{\Delta E}{kT_e}} \tag{2.24}$$

is growing fast with increasing electron temperature T_e and reaches its maximum at around $T_e \approx 2\Delta E$, which, according to an estimation for the mean ionization state [23]

$$Z \approx \frac{2}{3} \left(A \frac{T_\mathrm{e}}{[eV]} \right)^{1/3} \tag{2.25}$$

would no longer yield a significant abundance of the neon-like or nickel-like states. To overcome this, the transient pumping scheme is divided in two steps: first, a longer ($\approx$ ns) pulse creates a plasma column with an optimal abundance of the desired ionization state. Then, a short ($\approx$ ps), high intensity pulse heats the electrons to the necessary temperatures in a very short time, outrunning the ionization process and thus providing a narrow (a few to tens of picoseconds wide) window of gain which, owing to the high excitation rates, is considerably higher than in the QSS scheme.

2.5.1 *Traveling wave excitation*

With the TCE scheme, the usable target length is no longer only limited by the refraction effects as described before, but also by the gain lifetime which has to be long enough for the amplified pulse to travel through the gain medium. In order to be able to use target lengths more than a few millimeters (c times the gain lifetime), it becomes necessary for the gain region to move along with the pulse, which is possible using the so-called traveling wave excitation scheme. Practically, this means that the pulse front of the short pumping pulse must be tilted in such a way that it reaches the plasma only shortly before the arrival of the XRL pulse (see figure 4), which can be achieved by using gratings [40], step-like structures [41] or specific focusing geometries as for the experiments presented in this work.

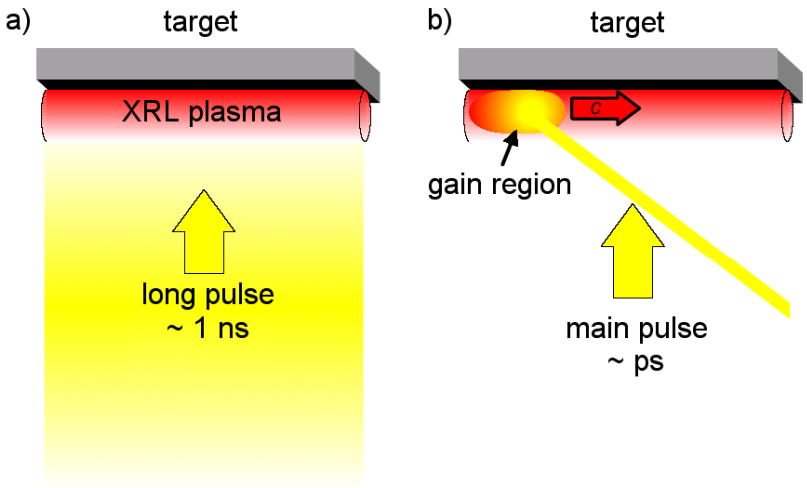

Figure 4: Scheme of traveling wave excitation: a long prepulse creates a preplasma (a) which is then heated by a high-intensity main pulse (b) just in the region where the population inversion is necessary for amplification of the spontaneous emission traveling through the plasma from left to right [20].

2.5.2 *Grazing incidence pumping (GRIP)*

Another problem to overcome on the way to highly efficient pumping schemes is the fact that generally, the energy of the main pulse is not deposited in the gain region of the XRL since the critical density (where most of the absorption takes place) is not automatically in the same region. The solution comes with the fact that a pulse with an incidence angle α against the target surface is reflected already at a density of [19]

$$N_r = N_c \cdot \sin^2(\alpha). \tag{2.26}$$

This gives control over the penetration depth and hence the region of energy deposition by variation of the main pulse incidence (GRIP) angle. Figure 5 shows plots of a simplified measure for the gain of a silver XRL obtained with the plasma simulation code EHYBRID [42] for plasma conditions very similar to those which were obtained in the experiments described in this work.

From this plot, the optimum density for pumping can be inferred to be around 2×10^{20} cm^{-3}, which together with the critical density for a 1054 nm (Nd:glass) laser, $N_c = 1 \times 10^{21}$ cm^{-3} leads with eq. 2.26 to a GRIP angle α of 26.5°. In the case of an 800 nm (Ti:Sa) laser, the optimal GRIP angle would be 19.8°.

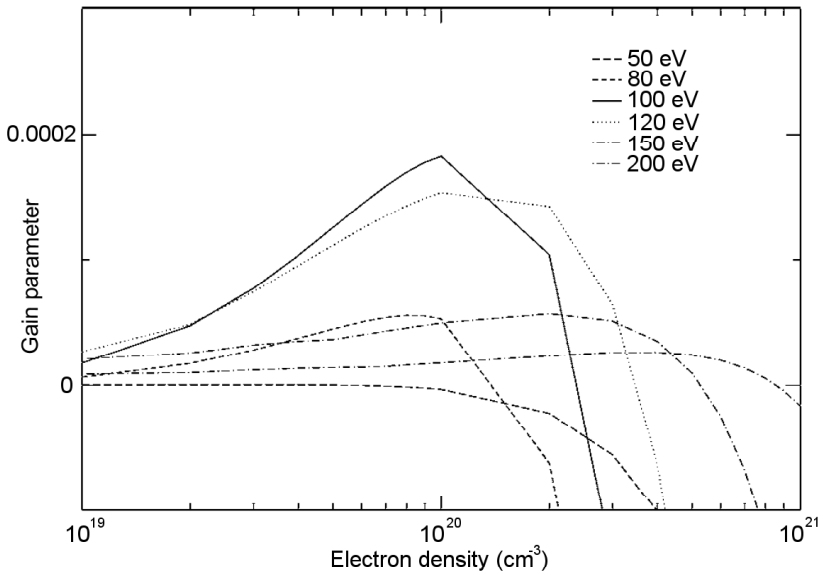

Figure 5: Plot of the steady state inversion parameter versus electron density for a silver XRL for different electron temperatures [43].

3 LASER SYSTEMS AND XRL SETUPS

3.1 THE PHELIX LASER SYSTEM

The *P*etawatt *H*igh *E*nergy *L*aser for *H*eavy *I*on e*X*periments system at GSI Darmstadt [44] [45] follows the so-called MOPA (*M*aster *O*scillator *P*ower *A*mplifier) design in which a weak (nJ) but very well-defined laser pulse is first generated by an oscillator. This pulse is amplified in several stages to higher energies (kJ) while retaining most of its other properties within the technical limitations. To achieve this with an acceptable power density in the optical components, the CPA (*C*hirped *P*ulse *A*mplification, [46]) technique is employed by stretching the pulse before the amplification in the time domain and re-compressing it after the amplification stages.

3.1.1 *The fs frontend*

The initial seed pulses are generated by a Kerr lens mode-locked Ti:Sa oscillator (Coherent Mira) with a center wavelength of 1054 nm and a spectral width of 16.5 nm, yielding 5 nJ pulses of roughly 220 fs duration with a repetition rate of 76 MHz. A single-grating, eight-pass Öffner-type stretcher [47] is used to extend the pulse duration up to 1.7 ns by guiding short-wavelength components of the pulse spectrum on a shorter trajectory than those with longer wavelengths and thus effectively spreading out the pulses' spectral components in the time domain. Single pulses are selected by a Pockels cell which injects them into a linear regenerative Ti:Sa amplifier at a down-divided repetition rate of 10 Hz, causing an amplification to about 5 mJ in 140 round-trips.

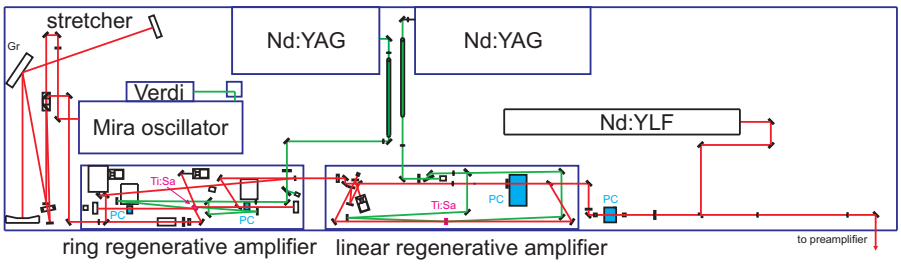

Figure 6: Overview of the PHELIX fs frontend (Gr: grating; PC: Pockels cell). The red lines represent infrared beams while the green lines show the pump laser beams for the oscillator and the regenerative amplifiers.

A second regenerative amplifier with a ring-shaped cavity raises the energy to up to 40 mJ in another 30 round-trips, the energy output for

daily operation is around 30 mJ. Figure 6 gives an overview of the present setup, a more detailed description can be found in [48].

3.1.2 *The preamplifier*

After a Pockels-cell based temporal cleaning and magnification to about 15 mm, the beam profile is spatially shaped by a serrated aperture and filtering in the focal plane of a relay telescope with a pinhole, producing a "top hat-"profile which can be described by a super-Gaussian function of order $n = 6...8$ in the form of

$$I(r) \propto e^{-(r/d)^{2n}} \tag{3.1}$$

for a given beam diameter d. The pulse to be amplified is guided (see figure 7) into two sequential 19 mm Nd:glass rod amplifiers which are separated by another Pockels cell to prevent parasitic lasing effects. Depending on the applied pumping flash lamp voltage, pulse energies of up to 1.3 J are thus available with a repetition period of 5 min given by the time the glass rods need to reach thermal equilibrium. Another magnification telescope images this pulse into a 45 mm Nd:glass rod amplifier which can be fired every 15 minutes, yielding energies of up to 5 J. A last telescope increases the outgoing beam diameter to nominally 63 mm which is the acceptance diameter of the PHELIX main amplifier section and the TW compressor, which will be described in the next section, as well. In the case of injection into the main amplifier, pulse energies of up to 500 J have been demonstrated at the present stage.

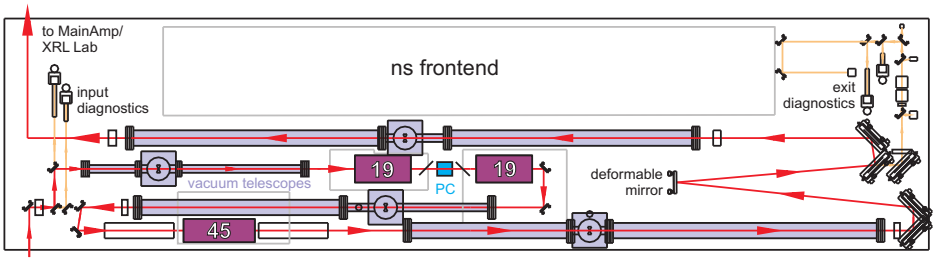

Figure 7: Overview of the PHELIX preamplifier. The yellow lines represent infrared beam leakages used for diagnostics.

3.2 THE XRL SETUP AT PHELIX

A 1:1 vacuum transport telescope images the preamplifier output beam over a distance of more than 20 m to the x-ray laser laboratory which is also situated in the PHELIX building's cleanroom class 10000 area. Most of the 125 mm high reflectivity (HR) mirrors are motorized and equipped with remote-controlled shutters and video cameras to allow for a fast

and reproducible alignment and the compensation of drifts in both the laser and the beamline.

3.2.1 *Combined compressor/delay line setup*

As can be seen on the overview scheme and in the photograph in figure 8, the beam is guided onto an 80×240 cm² optical table which is equipped with an aluminum housing and flow boxes to protect the sensitive optics from contamination caused by everyday construction work in the facility.

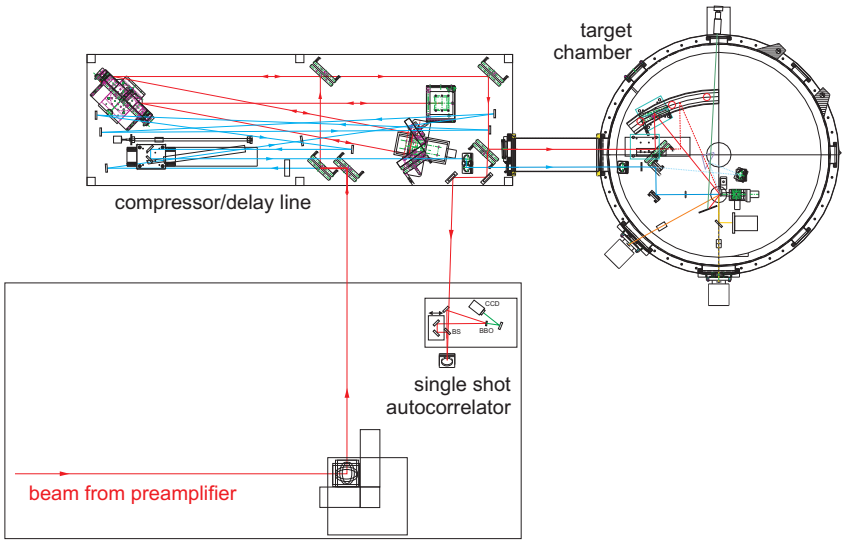

(a)

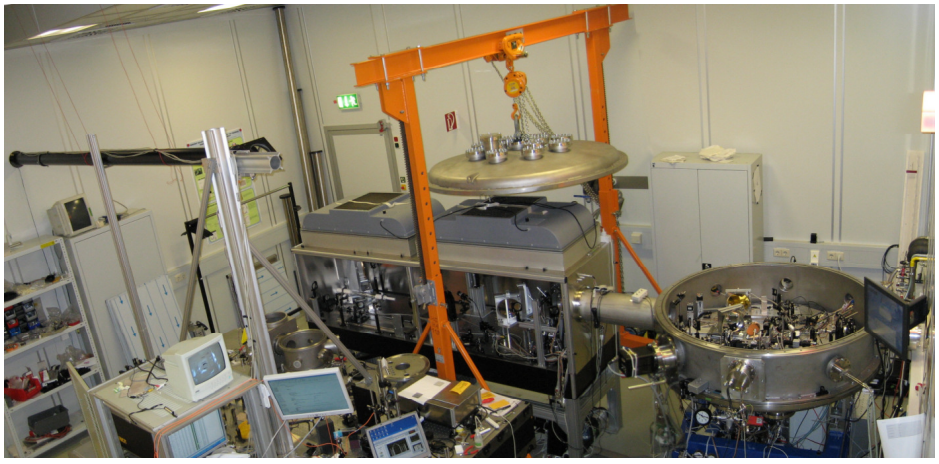

(b)

Figure 8: Schematic (a) and real (b) overview of the XRL laboratory setup.

Here, a fraction of 20 % of the energy is split off to remain uncompressed, while the rest enters a four-pass, single-grating optical compres-

sor which can be seen in detail in figure 9. The split-off beam (represented in blue) is reduced in diameter to about 22 mm by a Kepler telescope and sent to and fro between six 0° HR mirrors to compensate for the optical path which the other part of the beam has to travel through the compressor setup. At the end of this so-called delay line, two 45° mirrors, mounted on a motorized linear stage to allow the adjustment of the optical path over a length of 80 cm, reflect the beam towards a periscope which brings it to the same height as the compressor output beam.

The compressor consists of a 1480 lines/mm holographic gold grating on a 40 cm glass substrate and two sets of folding mirror assemblies which allow for a compact design and a simple alignment, details about the design can be found in [20]. One pair of folding mirrors can be moved on a motorized linear stage to change the compressor length and thus the duration of the compressed pulse over a range of 350 fs to more than 20 ps. The pulse duration can be monitored either via a motorized pick-off mirror for adjustment with the 10 Hz frontend beam or in single-shot mode using the leak through the last mirror before the target chamber entrance with a high-dynamic range autocorrelator which is described in detail in [49].

One important aspect of this setup is the fact that the optics for both beams are mounted on the same compact platform which makes it more robust against mechanical drift and furthermore facilitates the transport to and operation in other experimental areas at GSI (see chapter 5, [50]).

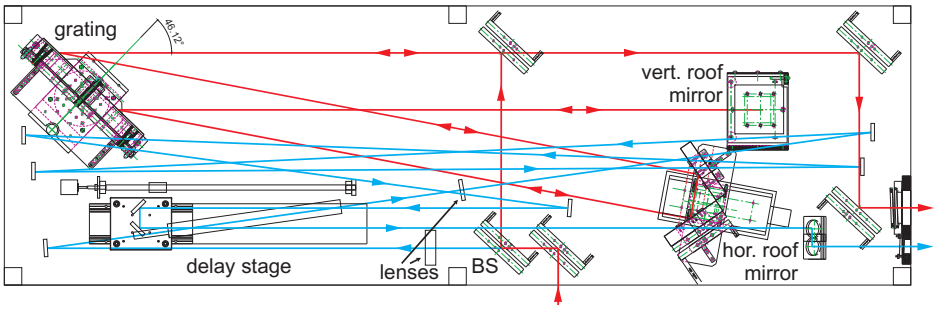

Figure 9: Schematic view of the compressor (red beams) and delay line (blue beams) setup (BS: Beam splitter).

3.2.2 *Target chamber setup*

FOCUSING OPTICS The target chamber which is located next to the compressor housing is a stainless steel vacuum vessel with 1.3 m inner diameter and an inner height of up to 45 cm. On the input side, it is extended with a stainless steel tube of 250 mm diameter, connecting it to the compressor housing, equipped with two slightly tilted, anti-reflective (AR) coated quartz windows for the uncompressed and the compressed

pulse, respectively. This solution allows for a rigid link between the compressor table and the target chamber and furthermore gives two well-defined input apertures, facilitating the alignment after compressor setup changes.

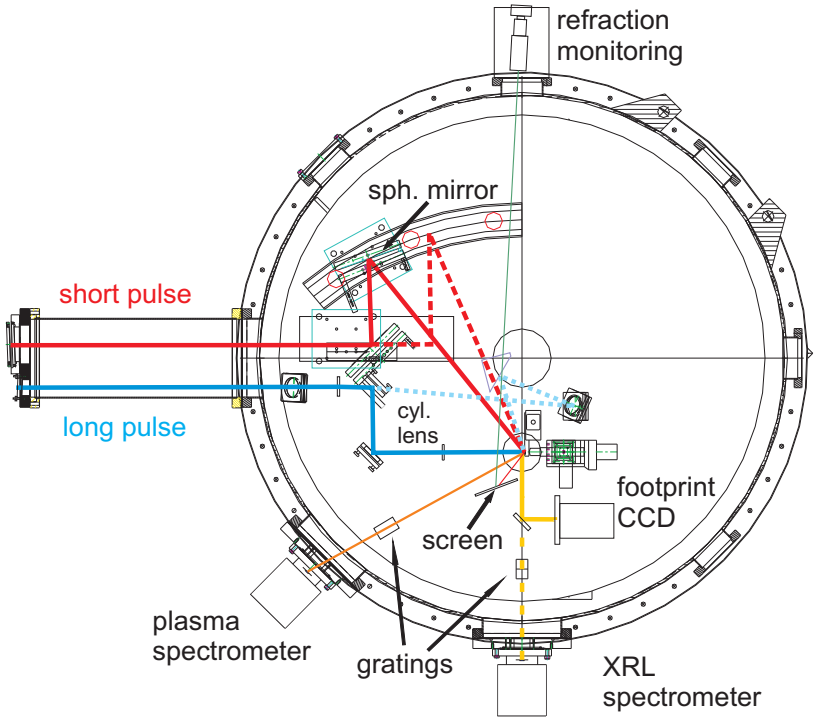

Figure 10: Schematic view of GSI XRL target chamber for the two extreme cases of main pulse incidence angle and the two beam paths for the uncompressed pulse.

Inside the target chamber, an aluminum breadboard of 1.2 m diameter and 30 mm thickness serves as a rigid mounting platform for the optical components of the XRL setup. The lid of the chamber can be lifted with a gantry crane, allowing easy access for setup changes and alignment. Once the lid is closed, the chamber is evacuated by a 35 m^3/h dry scroll pump and a 400 l/s turbo pump, a combination which can reach a vacuum level acceptable for experiments (below 5×10^{-5} mbar) in about 90 min. However, due to the sensitive CCD cameras and thin metal filters, the pump-down is usually throttled down by a butterfly valve between the prepump and the turbo pump, which result in a pumpdown time of at least 3 h. For the experiments described here, the chamber was pumped down over night, leading to a pressure of less than 1×10^{-5} mbar at the beginning of the beamtimes.

As can be seen in the schematic view in figure 10 and in the photograph in figure 11, the two beams enter the chamber from the side and are reflected by 45° HR mirrors to opposite directions.

There are two options for focusing the uncompressed pulses onto the

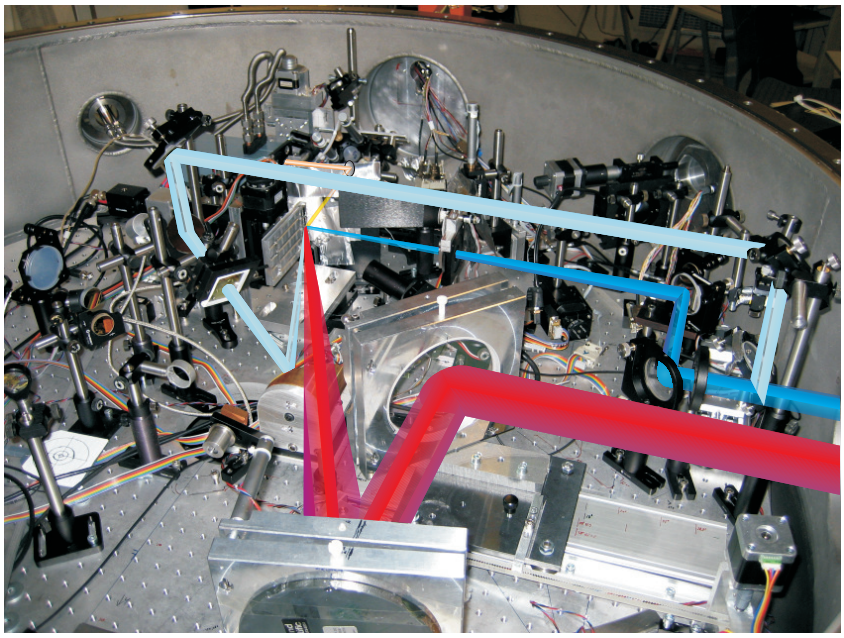

Figure 11: Image of the target chamber and the different beam paths for the compressed pulse (red), the perpendicular prepulse (dark blue) and the tilted prepulse (light blue) are drawn in together with the footprint output path of the XRL (yellow).

target which can be chosen under vacuum by moving a 45° HR mirror on a motorized linear stage. In the first one, the target surface is hit perpendicularly via an $f = 1000$ mm plano-convex and an $f = 250$ mm cylindrical lens, giving a line focus of 7 mm length and a width which is adjustable under vacuum in a range of 40–250 µm. The second option sends the beam upwards and then behind the target holder, from where it is sent downwards through an $f = 1000$ mm cylindrical lens onto a tilted 90° off-axis parabolic mirror which sends the beam under an angle of 65° and from below the plane of the other beams onto the target, again producing a line focus with roughly the same parameters.

The focusing of the compressed ("main") pulse is achieved by a tilted, gold-coated spherical mirror with $f = 600$ mm which produces a line focus of 6 to 11 mm length, depending on the angle of incidence on the target which can be varied from 24° to almost 40°. This scheme, apart from the ease of alignment as compared to other schemes using an on- and an off-axis spherical mirror (see, e.g., [51]), also provides an intrinsic pulse front tilt, resulting in traveling wave speed TW which can be shown [52] to follow

$$TW = \frac{1}{\frac{d\tan i_0}{f} \cdot \frac{\sqrt{1-(\sin i_0 - d/(4f))^2}\cdot\sqrt{1-(\sin i_0 + d/(4f))^2}}{\sqrt{1-(\sin i_0 - d/(4f))^2}-\sqrt{1-(\sin i_0 + d/(4f))^2}} - 1} \cdot c, \tag{3.2}$$

where i_0 is the incidence angle on the spherical mirror, f its focal length and d the beam diameter. With the parameters given in the setup, the traveling wave speeds were in the range of 1.1 to 1.4 c for 24° and 38.5° incidence angle, respectively. Again, this angle can be varied under vacuum by moving the spherical mirror and the preceding 45° HR mirror on customized linear stages. When changing the main pulse incidence angle, the spherical mirror is moved on a circular trajectory with a radius of 834 mm which is centered 236 mm below the target position as shown in figure 10. Since the spherical mirror is also rotated during this movement while still roughly maintaining its distance to the target, the remaining compensation in pointing and focusing can be achieved by linear actuators with only 13 mm movement range. Due to the LabView-based motion control interface, managing an overall number of more than 35 stepper motor axes, and pre-calculated positions from a simulation based on analytical geometry and ray tracing, a change from one angle of incidence to another can be accomplished in several minutes, maintaining the line focus position with a precision of better than 10 µm.

TARGET SETUP To allow for a reproducible and still flexible target replacement, a target holder (see figure 12) has been designed which can carry three different metal target slabs of up to 12 × 12 × 1 mm length and width and a frosted glass screen for the alignment of the line foci which can be moved vertically through the fixed line focus position.

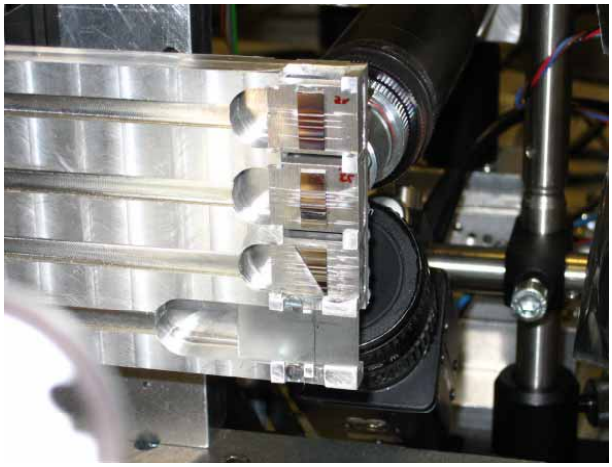

Figure 12: Image of the target holder with two straight and one triangular (gain curve) target. The glass screen at the lower end of the holder is imaged by two video cameras for easy and precise alignment of the line foci.

Since the targets are attached with instant adhesive onto replaceable support blocks which can be inserted into corresponding cut-outs in the target holder, a target change can be done in a short time without the need for realignment of the entire setup. The target surfaces and the

glass screen are flush with respect to each other within less than 30 µm (given the slabs were glued correctly which can be checked beforehand by a high-precision test gauge). This is important since the positions and geometries of the line foci are only checked with the 10 Hz frontend beam, using a video camera microscope with 1 µm resolution looking from behind the target plane at the frosted glass screen, which is afterwards moved downwards, bringing the target surface into the focal position.

DIAGNOSTICS In the early times of the GSI XRL setup, the primary diagnostics consisted of a flat field spectrometer with a curved grating (Hitachi 001-0437) and a back-thinned XUV CCD camera (Princeton Instruments NTE) mounted on a side port of the target chamber, oriented along the target surface and with a spectral resolution of $\Delta p/p \leq 2 \times 10^{-3}$ in a range of 6.5 to 26.8 nm. This allowed the verification of the both bandwidth-wise and also spatially narrow profile (due to so-called gain narrowing) which is typical for the emission of a plasma-based XRL, clearly distinguishing it from the sometimes also spectrally structured, but spatially unguided plasma emission. Later-on, this was replaced by an in-vacuum back-thinned XUV CCD (Andor DX-420) on which the XRL beam was guided with a multilayer 45° XUV mirror. While the spectral selectivity, given by the bandwidth of the multilayer mirror (about 1.5 nm) and the transmission characteristics of the employed metal filters, was not comparable to the one given by the flat field grating, it enabled the imaging of the farfield beam profile in two dimensions, i.e., to see what the XRL footprint actually looks like.

Due to their high sensitivity to visible light, both cameras were equipped with metal filters close to the CCD chips, which were selected to have spectral transmission windows for the desired XUV wavelengths. Especially for experiments requiring a high dynamic range of the diagnostics system like the recording of gain curves (see chapter 4.2.4), a set of metal filters of various thicknesses (0.5 to 2 µm) is mounted on a filter changer wheel positioned shortly after the target in the XRL beam path. An additional filter could be moved in the XRL beam with a motorized linear stage close to the footprint CCD, resulting in a variable attenuation from none to 6×10^{-3} for the Zr XRL using Al filters and up to 2×10^{-8} for the Pd XRL using Zr filters.

To learn more about the plasma states involved, a second flatfield spectrometer with a spectral range of 1.5 to 5 nm was installed, monitoring the plasma emission at an angle of roughly 45° to the target surface. It was read out with the same XUV CCD camera that was used before for the XRL spectrometer and yielded usable spectra at preamplifier energies starting from 800 mJ. Additional information on every shot was provided by a pinhole video camera (Pulnix TM-765E), giving the rough shape and informations about the homogeneity of the plasma line. Furthermore, an IR-sensitive firewire camera (Basler a302f) was installed, monitoring the

shape of the refracted pump laser beam after the interaction with the plasma looking through a glass window with a strong zoom objective at the upper side of the target chamber in figure 10.

3.3 THE LLC SYSTEM

The Lund multi-TW laser system resembles the PHELIX frontend system in several ways. It is also based on CPA, starting with a short-pulse, Kerr-lens mode-locked oscillator, but due to the different central wavelength of 800 nm which is closer to the optimal amplification wavelength of Ti:Sa, the pulse duration is as short as 20 fs. Before entering a grating-based stretcher, the pulses can be shaped by a Dazzler based on acoustooptic modulation.

The stretched pulses with a duration of 300 ps enter the first amplification stage at a down-divided repetition rate of 10 Hz. It consists of a regenerative Ti:Sa amplifier which increases the pulses' energy from tens of pJ to several mJ after eleven round trips in its cavity. After two Pockels cells which limit the ASE, the pulses are further amplified by a multi-pass Ti:Sa system to about 300 mJ per pulse which can then be divided in two parts, one of which can be sent directly to the compressor or target chamber. The other part, after a spatial filter stage to improve the beam quality and an expansion of the beam diameter to limit intensity-dependent beam degradation effects, is delivered to another multi-pass amplifier which is pumped at 10 Hz by 5 J of frequency-doubled Nd:YAG laser light and thus cryogenically cooled down to 100 K.

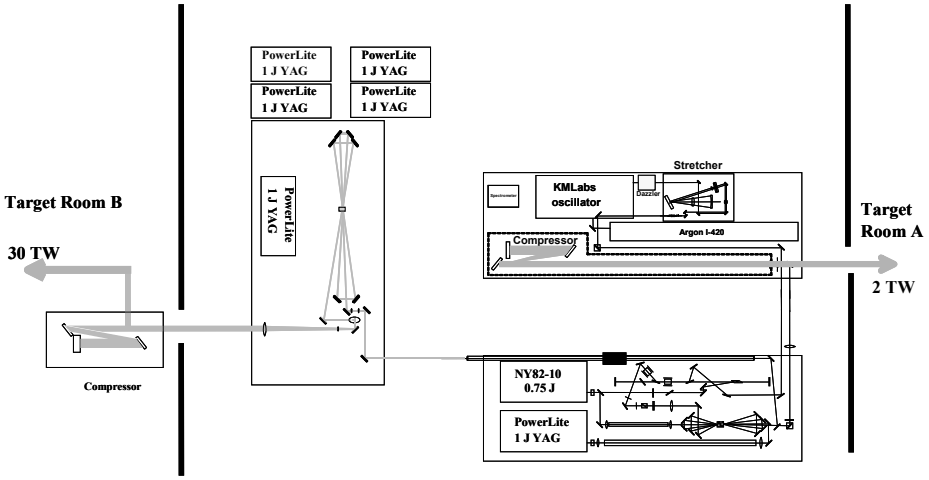

Figure 13: Schematic view of the LLC laser system. The experiments described in the next chapter were carried out in Target Room B, where also the compressor is situated. Image courtesy of F. Lindau, LLC.

At its output, the still chirped pulses have energies of around 1.5 J each, and are, after another increase in beam diameter to 50 mm, sent into a grating-based compressor housed in a vacuum chamber, which restores the pulse duration to 35 fs, resulting in a peak power of roughly 30 TW. An overview of the laser system can be seen in figure 13.

3.4 THE XRL SETUP AT LLC

3.4.1 *XRL setup*

The XRL experiments were performed in a vacuum target chamber of 1.2 m diameter and 40 cm height. In difference to the experiments at PHELIX, the uncompressed 300 ps prepulse was split up into two pulses with variable delay and energy ratio, but these two were combined again to travel the same path of a delay line and then focused by a spherical and a cylindrical lens onto the target, which was a 4 mm wide Mo slab. The compressed pulse with a pulse duration of 5 ps was guided under vacuum from the compressor onto a set of 45° HR mirrors and an on-axis (but used off-axis) spherical mirror, producing a line focus of 40 µm width and a length of 5-9 mm, depending on the GRIP angle which could be varied from 13° to 21°. A schematic overview of the setup can be seen in figure 14.

The XRL radiation generated in the plasma was focused by an on-axis multilayer imaging mirror onto a flat multilayer mirror and then projected through a 3.5 m long vacuum tube onto a back-thinned Andor XUV CCD camera, producing an image of the XRL exit plane with a magnification of 7.6.

3.4.2 *Pinhole camera setup*

The GRIP scheme is based on an optimization of the penetration depth of the pump laser beam into the plasma, which lead to the idea for a high-resolution diagnostic with the ability to yield information about the position of the hottest region in the plasma. Earlier experiments (see, e.g., [20]) have shown that the XRL plasma is a source for keV radiation which can only be created at high plasma temperatures. A setup was conceived which was able to determine the keV emission profile perpendicular to the target surface and which is depicted in a side view in figure 15.

It consists of a pinhole camera which can be positioned directly above the target in order to achieve the highest sensitivity for the distance between the target surface and the plasma, read out by a back-thinned XUV CCD (Andor DO-420) with 26×26 µm² pixels. The keV emission from the plasma was coming upwards along the target surface through a 1.4 mm opening in the target holder.

Since the entire target and its holder could be moved up and down

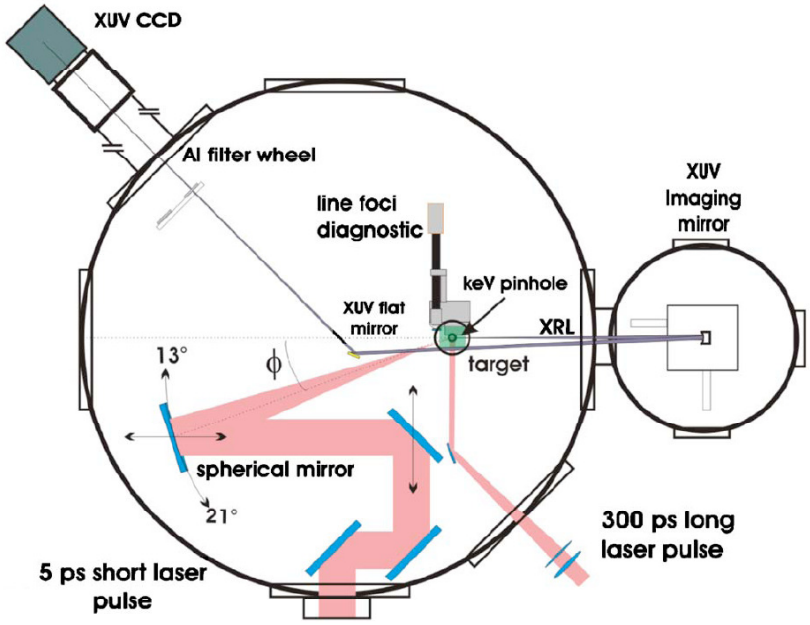

Figure 14: Schematic top view of the XRL setup at LLC. The two infrared laser beams are entering the chamber from below and lower right, the XRL output beam is imaged back from outside the right of the chamber onto a flat mirror and then sent along a vacuum tube onto a CCD camera [53].

by 40 mm to change the target surface, also the pinhole height had to be adjustable under vacuum in order to make use of the highest possible magnification. To facilitate the alignment, pinholes of sizes from 5 to 100 µm were mounted on a changer which in turn could be moved in the horizontal plane to compensate for movements resulting from changes of the pinhole height.

For the position measurements presented in chapter 4.1.2, a pinhole diameter of 8 µm was used together with a filter consisting of 1 µm polypropylene with two 100 nm layers of aluminum positioned about one millimeter above the pinhole, blocking radiation below about 600 eV. The magnification of the imaging system is determined by the distances between the plasma, the pinhole and the CCD chip and can be varied with a linear actuator between 9 and 27.

Although the *imaging* resolution of such a system is limited by the sizes of the CCD pixels and the pinhole, the *position sensitivity* can be considerably higher than this, because the position of a small light source can be determined much more precisely than its shape (which for example is used in Stimulated Emission Depletion (STED) microscopy, see, e.g., [54]). Even at medium magnifications, a position sensitivity of less than two microns can be achieved.

A useful feature of this system is the fact that it is mounted on a flange

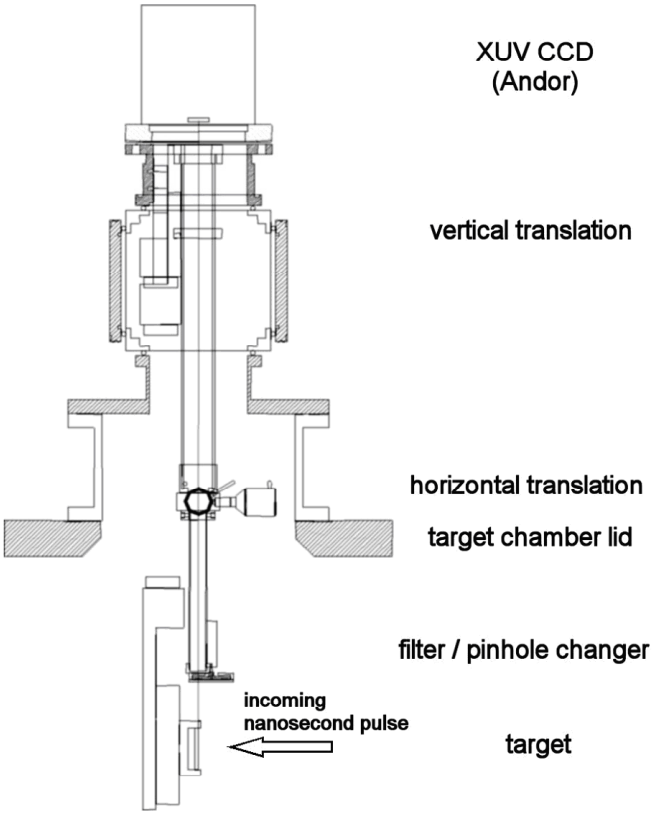

Figure 15: Schematic side view of the keV pinhole camera setup. It consists mainly of two pieces of tubing which are movable under vacuum and the front part which contains the pinholes.

on the target chamber and has no contact to parts inside which makes it more versatile than designs which rely on elements positioned, e.g., on breadboards inside the target chamber.

4 EXPERIMENTAL RESULTS

4.1 ANALYSIS AND OPTIMIZATION OF THE ENERGY DEPOSITION INTO THE PLASMA OF A NI-LIKE MOLYBDENUM XRL

4.1.1 *GRIP angle optimization*

Important results for this work were gathered during a European XRL campaign in Lund, Sweden, together with teams from Laserix, LIXAM, and the University of Paris Sud. Owing to the 10 Hz repetition rate of the pump laser system, a large number of shots could be taken, resulting in the investigation of a vast parameter space with a statistical uncertainty which is considerably lower than in previous experiments with lower repetition rate. These scans included the variation of the energy ratio between the compressed and the uncompressed pulses and their delays, the total pump energy, a scan of the GRIP angle and various settings for a prepulse preceding the bulk of the uncompressed pulse which lead to a considerable increase of the XRL brightness. The results of the GRIP angle scan are summarized in figure 16.

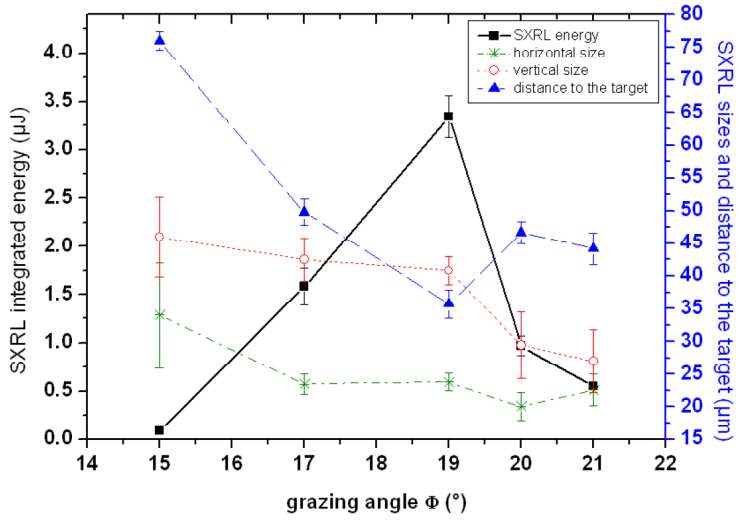

Figure 16: Effect of the GRIP angle on the XRL output energy, source sizes and position relative to the target surface [55].

A clear optimum in the XRL output energy is observed for a GRIP angle of 19°, and the smallest distance to the target surface is also measured at this angle. This can be seen as a proof of the benefits of the GRIP scheme, since eq. 2.26 predicts a deeper penetration of the main pulse

with increasing GRIP angle, moving the region of absorption, which for small GRIP angles is very far away from the target, closer to the density region of highest gain (see paragraph 2.5.2). At the same time, the position of the XRL source should be shifted closer to the target and, due to the higher gain, increase in intensity, which is indeed the case. For higher angles, though, the refraction due to steeper plasma gradients becomes stronger, resulting in an emission movement away from the target and a decrease in output energy. The energy at optimal conditions of roughly 3 µJ per pulse, together with the assumption of a pulse duration of 5 ps as measured in a similar experiment [56], corresponds to a peak spectral brightness of 10^{28} photons/s/mm²/mrad²/0.1 % BW [53].

When plotting the achieved XRL energy over the delay between long and short pulse for different GRIP angles, as it was done in figure 17, it can be seen that the optimal delay not only shifts towards shorter values for higher GRIP angles, but also that the delay range over which the best lasing operation can be achieved decreases steadily with increasing GRIP angle.

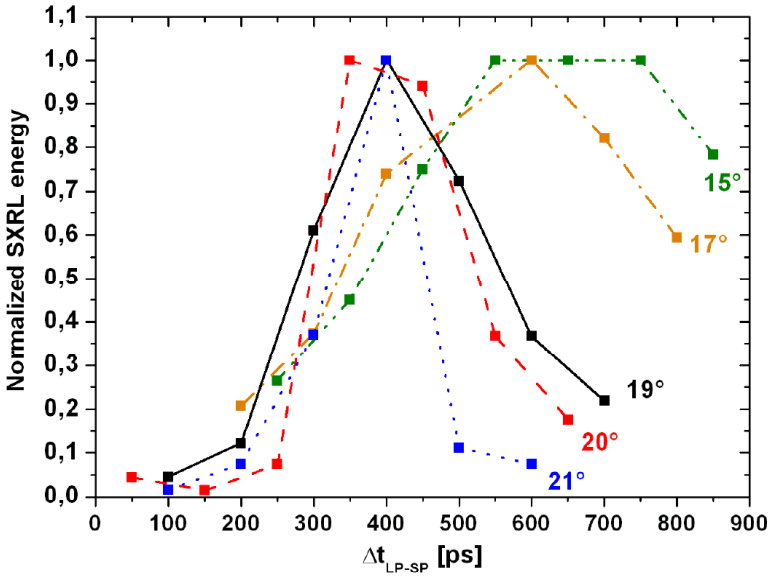

Figure 17: Normalized XRL output energies for different delays and GRIP angles [55].

The lack of XRL output at very short delays can be explained by the initially steep plasma gradients impeding the propagation within the gain region. Relaxation of this situation by cooling and expansion requires additional time. At higher GRIP angles, where the XRL is produced in a region with higher electron density, the recombination is faster, resulting in an earlier cool-down depletion of the lasing ion species, which leads to a more pronounced cut-off for those angles with increasing delay.

4.1.2 *keV pinhole imaging*

The pinhole camera described in chapter 3.4.2 yielded direct information about the energy deposition in the plasma plume by observation of the keV emission profile perpendicular to the target surface [57]. A typical image taken by the CCD camera is shown in figure 18.

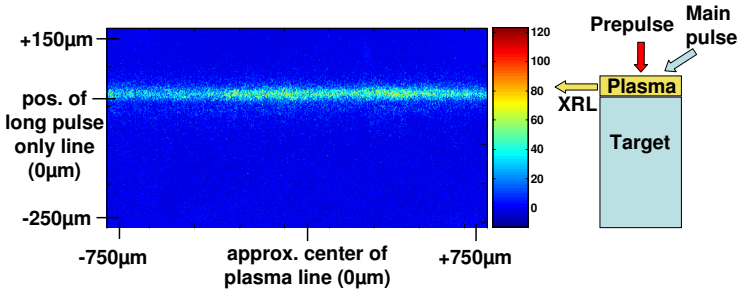

Figure 18: Image of the keV emission taken with the pinhole camera together with a scheme of the geometry for orientation.

The raw data for each shot were background corrected and vertically averaged cross sections were calculated, yielding curves of the average emission above 600 eV, selected by the filter, as shown in figure 19.

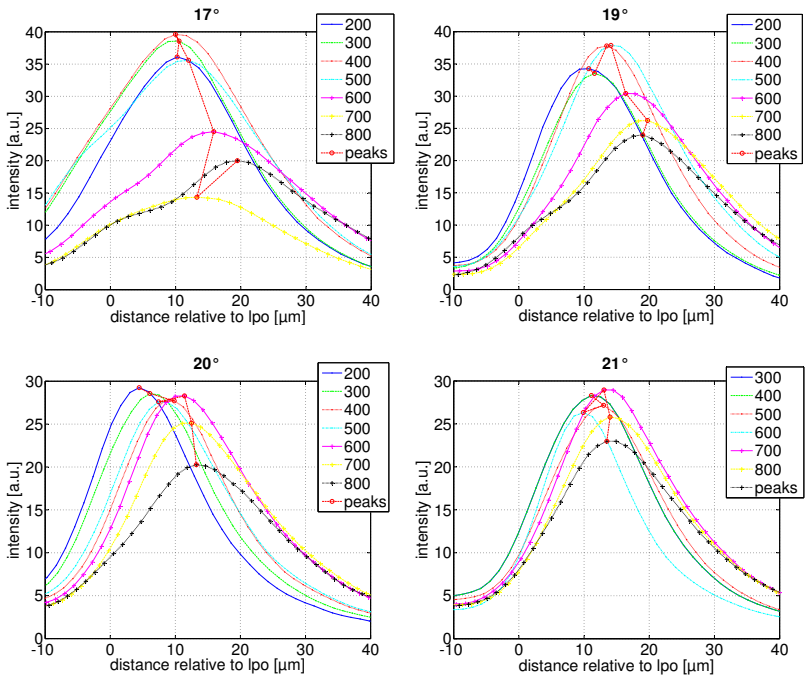

Figure 19: Cross section plots giving the keV emission profiles for different delays and GRIP angles relative to the peak positions of long pulse only (lpo) shots.

Due to the high magnification, the camera is roughly as sensitive to small long-term drifts especially of the pinhole position as to "real" plasma peak emission movement. It therefore is necessary to reference the peak emission positions to those of shots where the plasma was created only by the long pulse. For these shots, the plasma positions have been found to be rather unaffected by changes in the laser parameters, but show naturally the same dependence on long-term mechanical drifts, thus providing a first-order compensation for these deviations. The target surface itself could not be seen on the CCD images due to the strong attenuation of the employed filter. Although this means that the positions obtained here are only relative, an estimation of the absolute distance can be given based on the distance measurements from the near field imaging of the XRL output. Figure 19 shows the cross section plots for four different GRIP angles; for each delay, the average of at least six (usually nine or ten) shots was taken.

From the mean peak positions, values for the positions of the hottest points can be deduced, which are shown in figure 20 as a function of the GRIP angle.

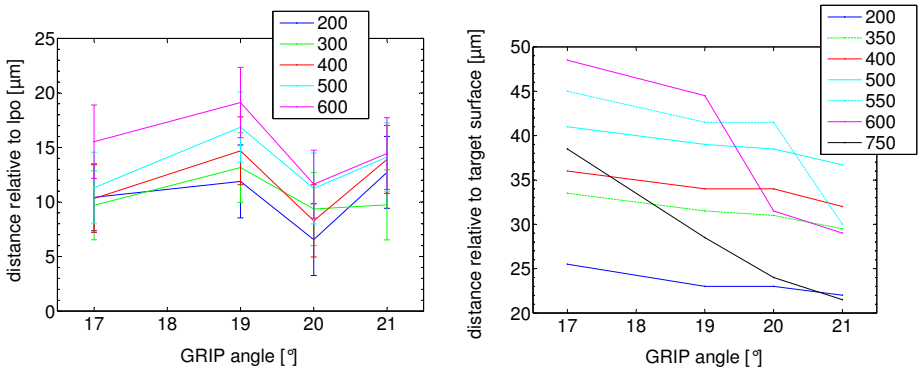

(a) (b)

Figure 20: Left side: Peak positions from the curves in figure 19, plotted over the respective GRIP angles for different delays in ps. Right side: Peak positions from an EHYBRID simulation in corresponding colors where data were available (otherwise dashed curves) for different delays in ps.

Using the simulation code EHYBRID, the positions of the keV emission peaks can also be estimated, which is shown in the same figure on the right side.

The keV peak distance to the target shows a behavior similar to the movement of the XRL emission aperture position in figure 16, although the angle where it is closest to the target is shifted by one degree. A possible reason for this might be a mismatch between the position of the

keV and the XRL emission, since, according to

$$N_r = N_c \cdot \sin^2(\alpha), \tag{4.1}$$

a GRIP angle difference of 1° equals to a shift of less than 10 % in the electron density encountered by the pump beam. It might also result from short-term thermal drifts which were not detected by the long-pulse-only reference shots and which, due to the high resolution of the system, can have a notable effect. Further investigation with improved reference procedures to detect and correct for setup drifts is needed to clarify this.

The keV peak data points are plotted again in figure 21 as a function of the delay between long and short pulse, together with the data derived from the simulation which show a drop-off for longer delays which shifts towards smaller delay values for higher GRIP angles.

Looking at the peak positions from the plasma expansion point of view, at a longer delay, the short pulse hits the plasma created by the long pulse at a later stage of the expansion of the plasma plume. Therefore the slopes of the position fits in figure 21 can be interpreted as the expansion speed of the plasma.

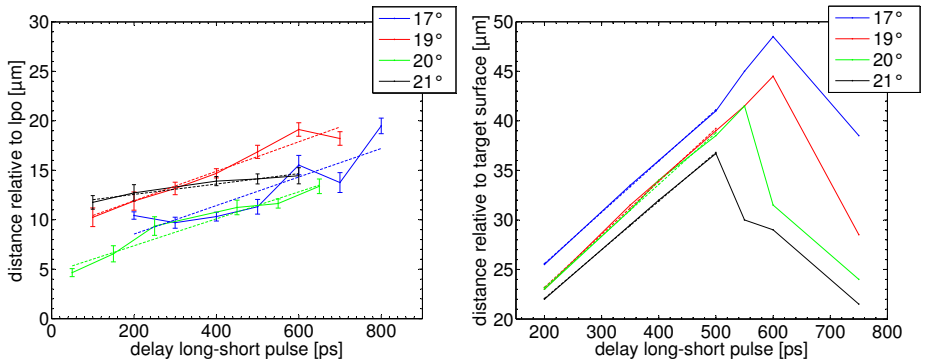

Figure 21: Peak positions, plotted over the long-short pulse delay. The dashed lines show linear fits to the data points for each GRIP angle. In the case of the simulation results on the right side, only delays up to 500 ps were taken into account for the fits.

Since each delay scan series for a respective GRIP angle was performed consecutively in a relatively short time interval, they have the advantage of being less sensitive to long-term drifts of the setup, which would cause a vertical shift of the plots, but leave their slopes relatively unaffected. These slope values are shown in figure 22, together with the result from an EHYBRID simulation.

The comparison with the simulation data shows qualitative agreement, although the overall speed values are deviating by a factor of almost 4. This indicates that the heated region moves slower than expected for the turning point of the pump beam. In turn this implies that the heated

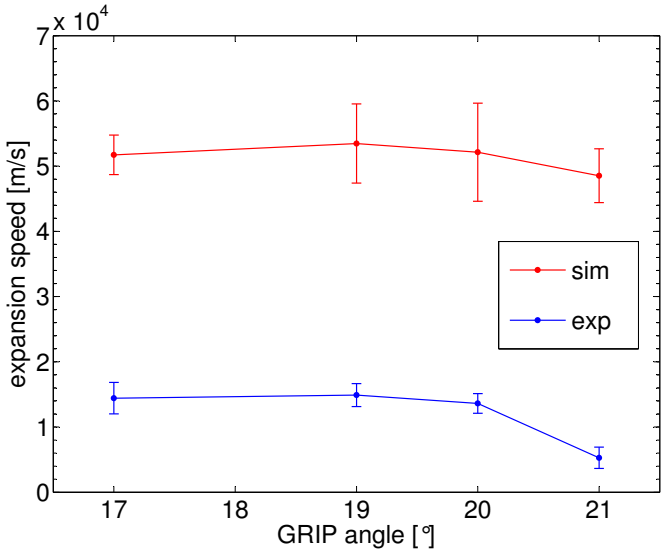

Figure 22: Slope values of the fits in figure 21, interpreted as displacements in the time of the respective delays, from the experimental data (blue) and the simulation (red). The error bars represent the fitting uncertainties.

region in the plasma actually is placed at higher densities, in the deeper part of the plasma region, a fact that is potentially beneficial for the approach to shorter wavelength XRLs, where the necessary gain requires to work in a region of higher plasma density. Such a heating closer to the target, in a plasma region that cannot be directly reached by the pump beam, is possible due to heat transfer by hot electrons generated by the laser interaction. The evidence provided by the new data is an important hint for the usefulness of this process for pumping multi-100 eV plasma x-ray lasers.

4.1.3 *Target usage considerations and high-repetition rate operation*

A major obstacle for the continuous operation of an XRL based on plasmas originating from solid targets is the fact that each shot consumes a certain amount of target material, creating a crater which sooner or later necessitates the change of the target surface which is an ultimate limit for long-term operation. Measurements of the movement of the XRL source and analysis of the target surface after the experiments have shown that that in the given case (Mo, 1 J total pump energy per pulse), each shot ablates a layer of about 0.25 µm [58]. The proof of the capability for reliable 10 Hz XRL operation was accomplished by taking two series of 100 consecutive shots each. In the first series, the target moved continuously at a slow rate, while in the second one, the target

remained stationary. As can be seen in figure 23, the case of the stationary target not only shows the better overall output performance, but even an improvement in the second half of the series.

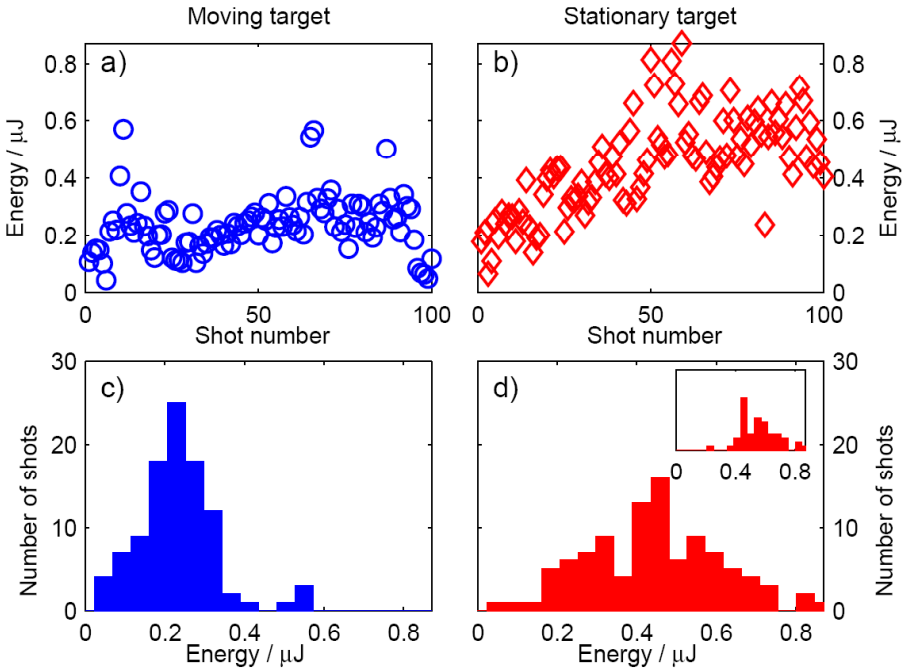

Figure 23: XRL output energy time series and histogram for moving target, a), c) and stationary target b), d). The inset in d) is the histogram for the last half of the shot sequence. The mean energies are 0.22 µJ and 0.42 µJ for moving and stationary target, respectively [58].

This can be explained by the formation of a groove in the target surface which can act as a guide for the pump beams and effectively impede the plasma expansion in the vertical direction since after 50 shots, the groove depth is already more than 10 µm.

4.2 ANALYSIS AND OPTIMIZATION OF THE ENERGY DEPOSITION INTO THE PLASMA OF NI-LIKE ZIRCONIUM AND PALLADIUM XRL

The outstanding results from the LLC experiment encouraged further investigation concerning their applicability to systems with a shorter XRL wavelength, and to the PHELIX XRL system. A repetition rate 10 Hz is, due to the Nd:glass rods' cooling time, beyond the reach of the PHELIX system in its current state (although so-called zigzag slab glass amplifiers have recently shown stable operation at 0.1 Hz [59]). Still, a lowering of the pump energy requirements would be beneficial since, as has been said before, shooting with only the preamplifier's 19 mm heads instead of all three heads increases the repetition rate by a factor of three. A further enhancement of the repetition rate as high as one shot per minute is conceivable by the introduction of fixed shot cycles using the relatively stable cooling curve of the glass rods.

4.2.1 *Zr, Mo, Pd and Ag XRL*

Figure 24 gives a pictorial overview of the different XRLs which were achieved with the PHELIX setup with their peak heights normalized to similar values for ease of comparison. For the same reason, the plotted spectra were not taken from shots with optimal XRL output since then, several thin metal filters were necessary to avoid saturation of the CCD-based detector, which reduced the spectral background so much that indeed solely the XRL emission peaks were visible.

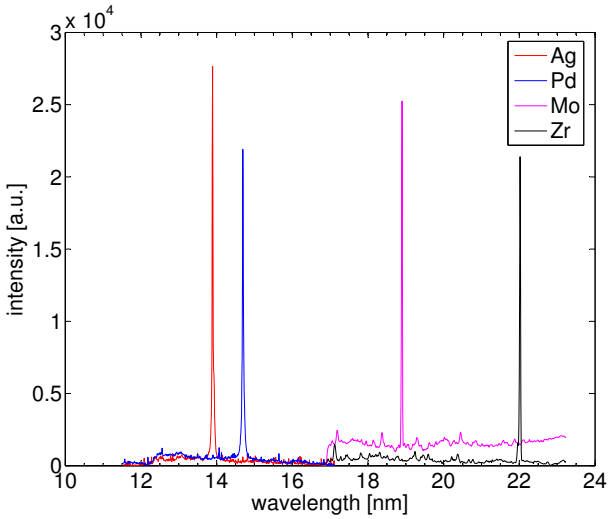

Figure 24: Compilation of spectra taken with the flatfield spectrometer at the output of the XRL during several beamtimes in spring 2007.

Although the XRLs based on all four materials could be accomplished reproducibly, the following chapters use mostly data taken with zirco-

nium. This was partly because for this material, several multilayer mirrors (although optimized for 21.2 nm, the lasing line of Ne-like Zn) were readily available which was not the case for molybdenum. As for the XRLs based on the heavier elements Pd and Ag, earlier experiments had shown that they depended on the use of pumping energies only available with the 45 mm head which made them less attractive for investigations with the need for many shots, although, as will be shown in chapter 4.2.8, at least for the Pd case, this constraint is no more mandatory.

4.2.2 *Influence of prepulse duration*

First attempts to investigate systematically the influence of the main pulse incidence (GRIP) angle and the delay between the two pulses showed only a very weak dependence of the XRL output energy on these parameters. For example, even with a delay of more than 2 ns, the XRL still showed significant output. The reason for this was found in a very successful improvement of the PHELIX frontend setup. This improvement had the aim to increase the bandwidth by introducing a narrow-band filter in the ring regenerative amplifier in order to precompensate gain narrowing in the following amplifier stages. While this worked very well for pulses which were fully amplified with the 45 mm head and the main amplifier, pulses amplified only by the preamplifier's 19 mm heads were stretched to a pulse duration of more than 2.5 ns which was much longer than the specified 800 ps of the time before the optimization. Figure 25 shows the result of a delay scan with the elongated and unevenly shaped prepulse.

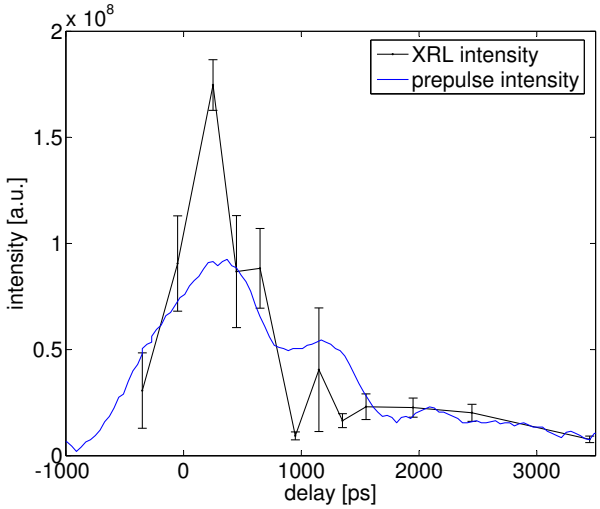

Figure 25: XRL output intensities for a scan of the delay between the uncompressed prepulse and the compressed main pulse at a GRIP angle of 25°. The blue line shows the intensity of the prepulse measured with a fast photodiode on the same time scale.

The direct comparison to the temporal prepulse intensity devolution which is plotted for reference in the same graph shows resemblances between the two curves, especially in the long low-intensity tail. Apparently, the XRL experiment in this sense was a correlation measurement between the two pulses, scanning the uncompressed pulse with the compressed one.

After a reconstruction of the old frontend setup, the prepulse shape regained its specified 800 ps FWHM width. The resulting delay scan curve is depicted in figure 26, together with the prepulse shape.

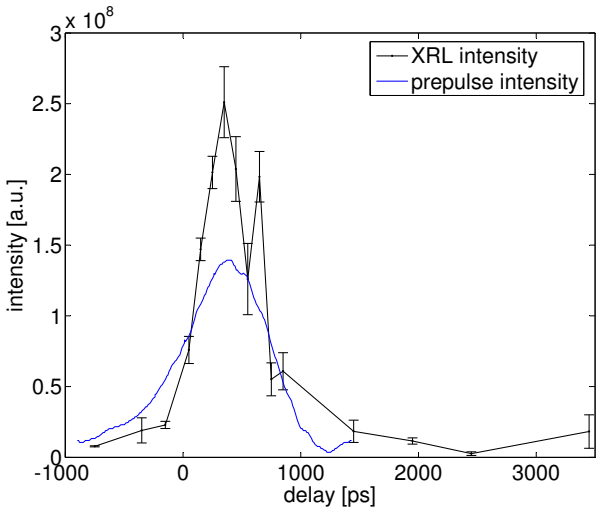

Figure 26: Delay scan with a shortened prepulse at a GRIP angle of 27°.

As can be seen, the FWHM of the delay curve is comparable to the duration of the uncompressed pulse, which was also the case in the LLC measurements close to the optimal GRIP angle.

4.2.3 *GRIP angle optimization*

As has been shown as an important result from the beamtime in Lund in chapter 4.1.1, there is a marked dependency of the XRL performance on the GRIP angle. The measurements presented there had the great benefit of having been taken with a high-repetition-rate (10 Hz) pump laser system which helped significantly to keep the uncertainties from shot-to-shot fluctuations low by averaging over a large number of data points. However, due to extensive optimization of both the pump laser system and the XRL setup stability, which resulted in a reliable XRL operation over periods of more than ten hours at a repetition rate of one shot every 4 min, it became possible to perform the same optimization again with another pumping laser type and a different lasing material. It should be noted that, due to the different central wavelengths of the two

laser systems (LLC: 800 nm, PHELIX: 1054 nm), the GRIP angles differ distinctly. The relation between the GRIP angles follows from eq. 2.26

$$\alpha_{\lambda_1} = \arcsin\left(\sin(\alpha_{\lambda_2})\frac{\lambda_1}{\lambda_2}\right). \tag{4.2}$$

For a silver XRL, the optimal GRIP angles are 19.8° and 26.5° for an 800 nm and a 1054 nm system, respectively.

An overall number of 160 shots during two beamtime days were performed, out of which about 25 were rejected because they were not in the specified pump energy range of 1100-1250 mJ and about the same amount was not or only weakly lasing, mostly due to fresh target surfaces. For each GRIP angle, a fresh surface position was used and it usually took three shots until the optimal performance was achieved. The trends of the respective delay optimizations become clearly visible by fitting Gauss curves to the acquired data, as can be seen in figures 27 and 28.

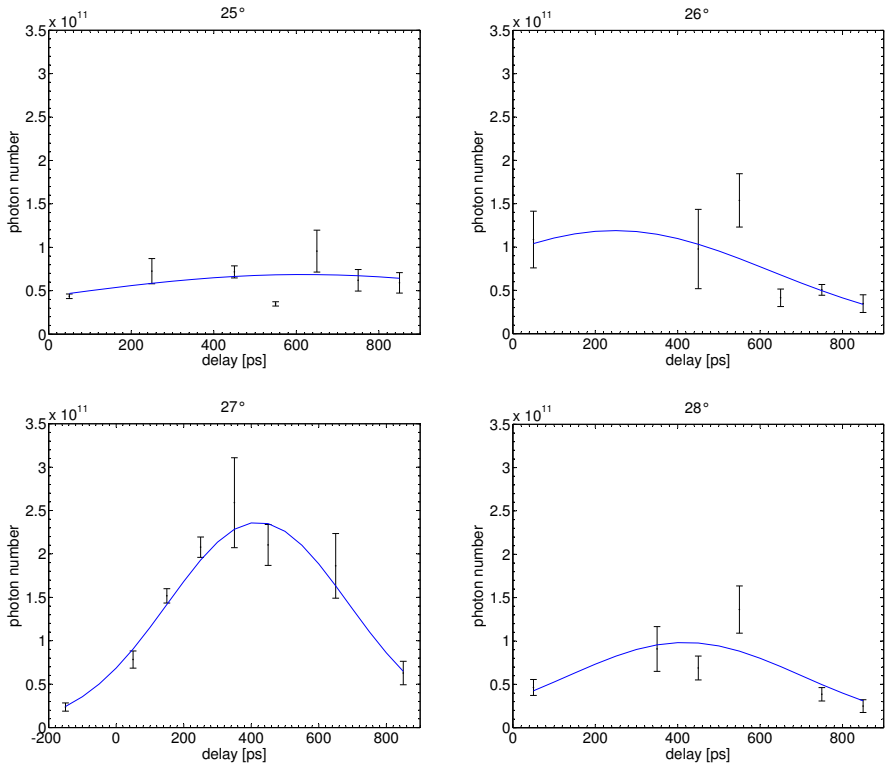

Figure 27: Delay scans for GRIP angles 25°-28° with their respective Gaussian fits.

As in all intensity measurements which were performed with the PHELIX system, the values were acquired from a background-corrected integration over the region where the XRL could be seen on the camera image, which for the measurements presented in this chapter was always

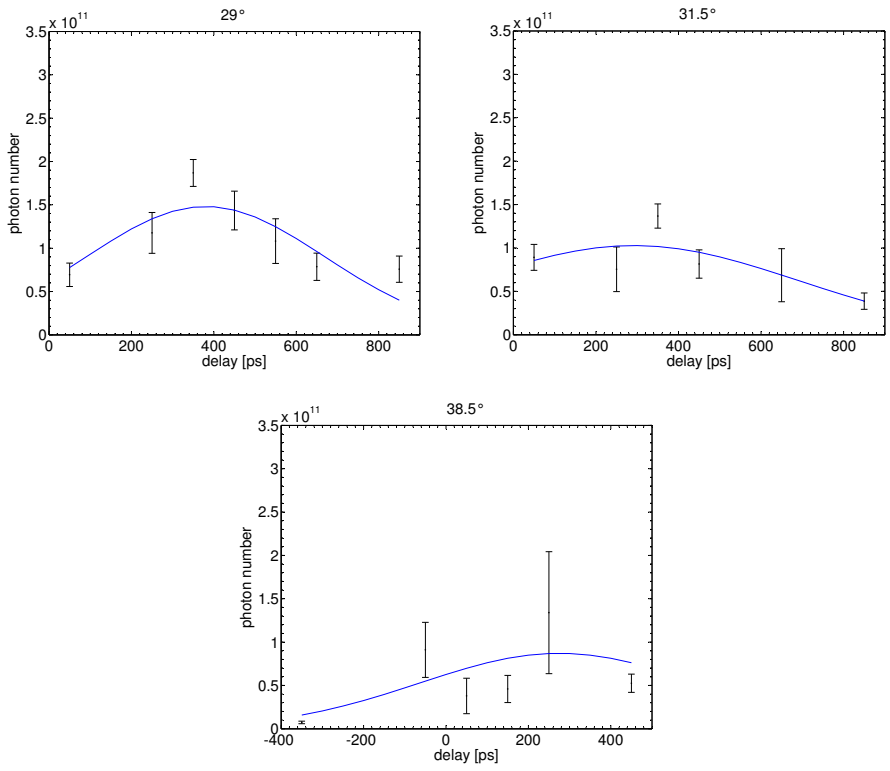

Figure 28: Delay scans for GRIP angles 29°-38.5° with their respective Gaussian fits.

in the center of the images. Even though the height of the CCD chip was only 6.6 mm, the entire beam profile could be registered without the clipping problems reported in earlier experiments [20], due to the comparably small XRL divergence.

For comparison of the best XRL performances for different GRIP angles, the peak values of the respective Gaussian fits are plotted against the angle in figure 29. Although the uncertainties are larger than in the LLC measurements, a significant dependence can be seen, showing an optimum at at GRIP angle of 27°.

To accentuate the correlation between GRIP angle and delay, the fitted curves are plotted again, normalized to the same intensity value in figure 30. Apart from the 25° peak which is distinctly broader than the other fits (which might be attributed to a lack of data points in the extreme delay regions), the fit curves are narrower in the region around the optimal GRIP angle at 27° and besides have their optimum at longer delay values.

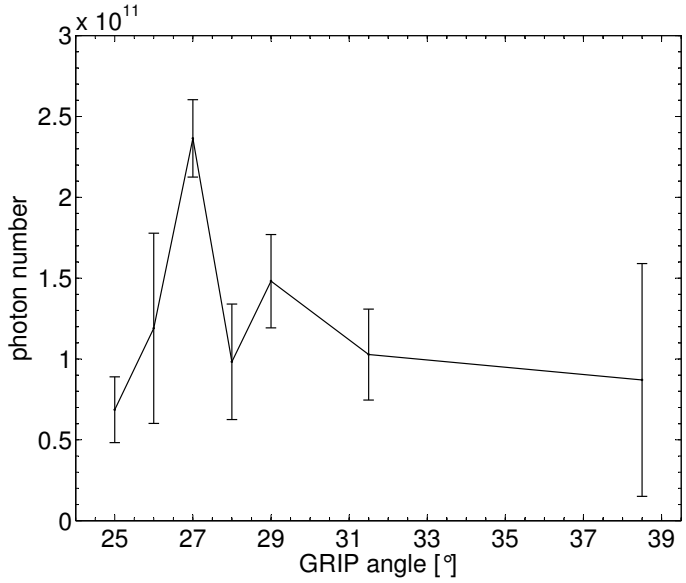

Figure 29: Gaussian peak values with their respective fitting uncertainties for different GRIP angles.

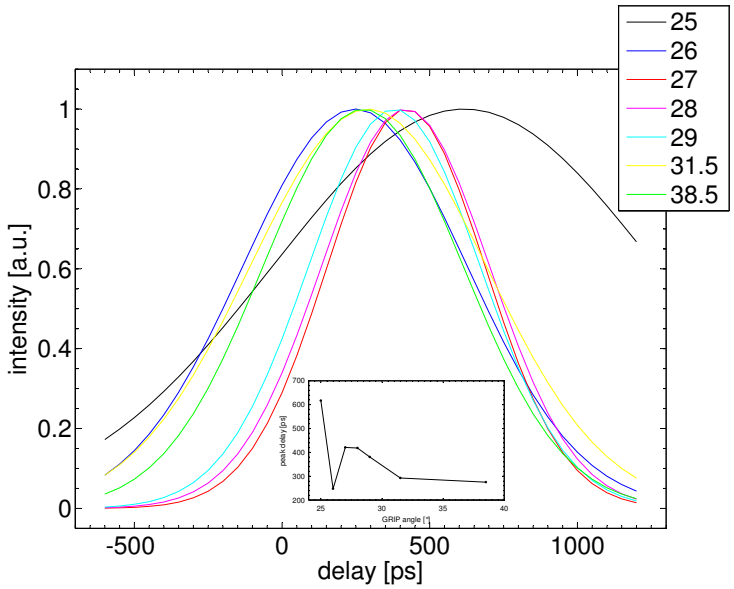

Figure 30: Normalized Gaussian fits for different GRIP angles in degrees. The inset shows at which delay the intensity peaks for each GRIP angle are situated.

4.2.4 *Gain curves*

As has been outlined in chapter 2.3, the characterization of the gain behavior of the pumping scheme under investigation gives an important benchmark. It has become common practice (see, e.g., [27] [60] [35]) to vary the target length and thus the length of the amplifying plasma column while keeping all other parameters constant and then find the point where the amplification reaches the saturation regime, usually visible as a roll-off in the exponential increase of the output energy with increasing target length. A practical way to vary the target length is the use of triangular targets as shown in fig. 31 since, compared to step-like targets, they allow an optimal choice of target lengths during the experiment to be sure to retrieve enough information about the roll-over region.

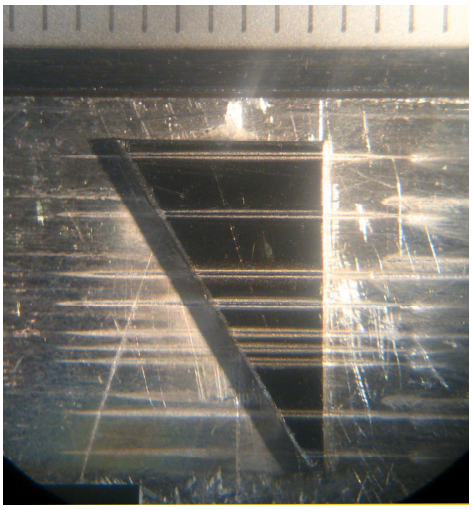

Figure 31: Microscope photograph of a well-used Zr gain curve target on its aluminum support. The plumes on the right edges of the line foci imprints on the support originate from pump laser light coming from the left which was refracted in the plasma plume. The plumes which are not situated at the end of an imprint line are caused by the optionally used non-normal incidence prepulse, incident on the target from below the plane of the other beams. The ruler on the upper edge gives a scale in millimeters.

Figure 32 shows a Zr gain curve acquired during two beamtimes with the PHELIX XRL setup with a prepulse duration of 3 ns.

A fit of the data points (blue line in figure 32) in the small signal gain regime with the Linford formula (see eq. 2.18) gives a gain factor of 6.7 /mm, which together with the saturation length of 2.8 mm results in a gain-length product of 19. The given photon numbers are calculated for the amount of XRL radiation in the beam profile, deduced from the integrated, background-corrected CCD counts and corrected for the

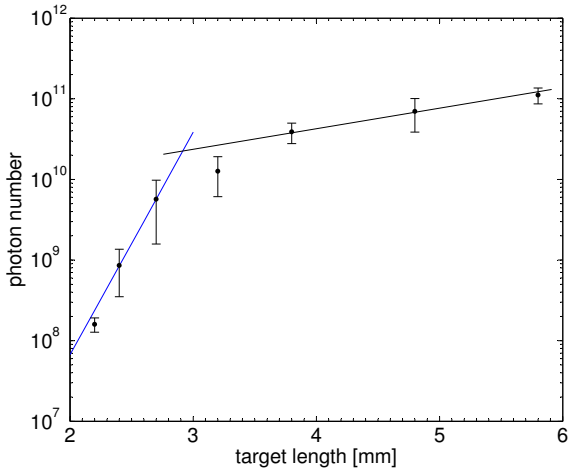

Figure 32: Gain curve of a Zr XRL taken with the PHELIX XRL in July 2007. The durations of the long and short pulses were 3 ns and 6 ps, respectively, their delay 130 ps at a GRIP angle of 25° with a total pump energy around 1 J. Each data point represents the mean of at least three shots with its respective standard deviation as error bars, except for the 2.2 mm where, due to the lack of data points, an error of 20 % was assumed.

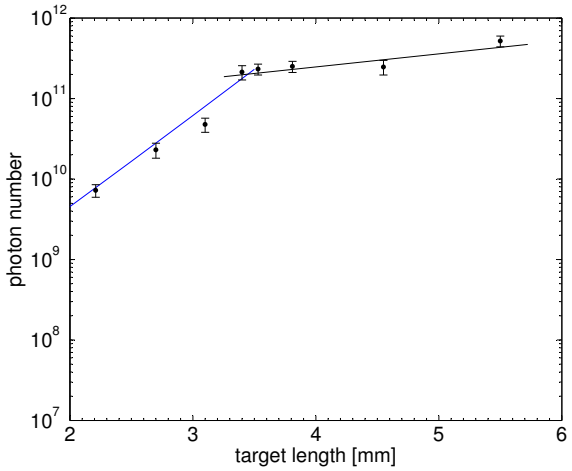

Figure 33: Gain curve of a Zr XRL taken with the PHELIX XRL in August 2007. The durations of the long and short pulses were 800 ps and 5 ps, respectively, their delay 450 ps at a GRIP angle of 27° with a total pump energy around 1.1 J.

filter transmissions and multilayer mirror efficiency. At a wavelength of 22.02 nm (56.3 eV), a photon number of 1×10^{11} corresponds roughly to 1 µJ laser pulse energy.

After a shortening of the prepulse duration to about 800 ps and a change to the optimal GRIP angle of 27°, the measurements were repeated

with an optimized delay and produced, as can be seen in figure 33, a much lower gain of only 2.8 /mm with a gain-length product of 10 in the unsaturated regime. However, the overall signal strength was increased by a factor of five, which can be explained by a more efficient deposition of the energy of the shortened long pulse into the plasma and the fact that the relaxation phase, necessary for lowering the density gradients, is not disturbed anymore by the "tail" of the long pulse.

4.2.5 *XRL farfield measurements*

The primary diagnostic of the PHELIX XRL setup gives a direct image of the beam profile at a distance of 31.5 cm from the target, usually referred to as "footprint". From the analysis of the CCD images, apart from the integrated photon number, information about the divergence and the XRL pointing deflection can be gained. Figure 34 shows typical footprints of shots under the respective optimal conditions for different GRIP angles.

The strong vertical modulation of the beam profile can be attributed to a double structure of the XRL nearfield which has also been observed in the LLC beam time under certain conditions [55] and other experiments (see, e.g., [61]). This can be seen from the good qualitative agreement with simulations shown in figure 35 performed at Université Paris Sud [56] for the case of a low spatial coherence, a high longitudinal coherence, and a short (6 ps) XRL pulse duration.

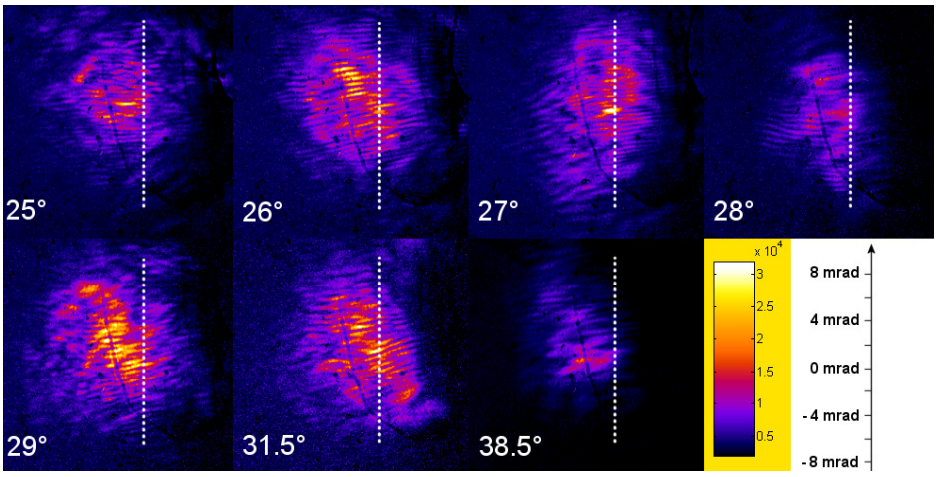

Figure 34: Near field images of the Zr XRL under optimal delay conditions at energies around 1.1 J for different GRIP angles. The dashed line marks the prolongation of the target surface, refraction in the plasma leads to a deflection towards the left.

For an evaluation of the position and deflection, the footprint images were smoothed and fit with Gaussian profiles. Figure 36 shows the trends

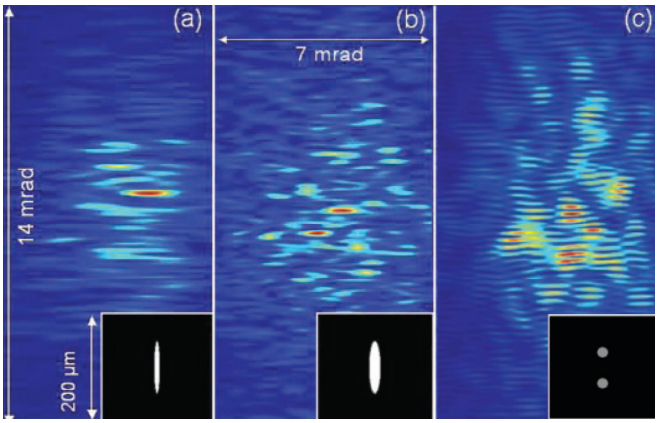

Figure 35: Simulated near fields for various exit aperture shapes (insets) with XRL pulse durations of 6 ps and a coherence time of 2 ps. Images courtesy of O. Guilbaud, Université Paris Sud.

already visible in the images in figure 34, especially the low deflection around the optimal GRIP angle.

With increasing GRIP angle, the deflection becomes weaker with a minimum around 27°, and increases again for higher angles, while the beam divergences in both directions have maxima at 27° and the vertical divergence increases again for the highest GRIP angle. A stronger deflection at higher GRIP angles can be explained by the notion that there, the main pulse beam can penetrate deeper into the plasma which results in steeper density gradients, increasing the refraction. The overall deflection is low compared to earlier experiments (see, e.g., [20]), which can be accounted to the under-dense plasma regime associated with the GRIP scheme.

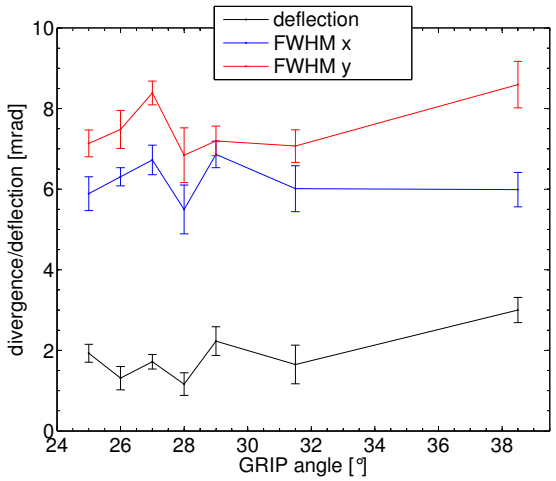

Figure 36: Divergences and deflections from the target axis deduced from the footprint images for different GRIP angles.

4.2.6 *Imaging of the refracted pump laser beam*

Several XRL experiments at different facilities around the world (see, e.g., [62]) involving compressed beams hitting the targets under strongly non-normal angles revealed an interesting side-effect: on the first aperture in the XRL beam or even on the walls of the target chambers, sickle-shaped imprints (see, e.g., figure 37) became visible after extensive beamtimes.

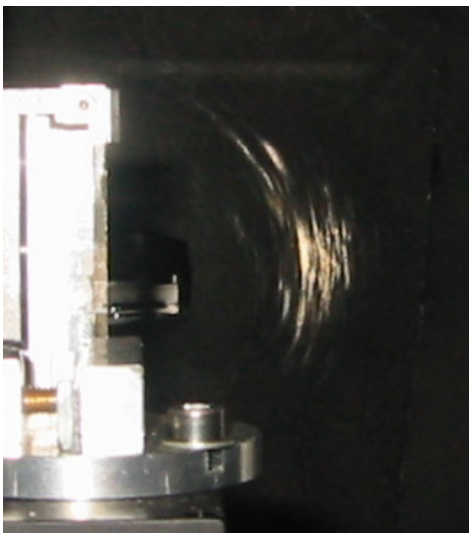

Figure 37: Photograph of the anodized aluminum sheets along the wall of the target chamber at LLC (placed there to absorb plasma stray light) after the experiment. On the left side, the Mo target slab can be seen, while the imprints of the pump laser are clearly visible, centered around the exit trajectory of the XRL beam.

From the geometrical proportions it can be assessed that they are caused by the main pulse beams which are refracted strongly in the plasma or on the target surface while still retaining enough intensity to cause surface damage on anodized aluminum even in their divergent states. To learn more about this effect, a rather simple diagnostic was developed at the PHELIX setup. It consists of a 1 mm plate of roughened and anodized steel, positioned at a distance of about 15 mm to the XRL output beam, imaged through a window at the back side of the target chamber with an 8-bit monochromatic firewire CCD via a strong zoom objective and an infrared-selective filter. As can be seen in figure 38, detailed profiles can be achieved.

A profound investigation which requires a ray tracing analysis based on plasma simulation codes is still in preparation. But already the fact that there seems to be a significant deviation of the recorded pattern positions to the ones which are expected from the simple relation of input equaling output angle shows that the setup described here can provide interesting insights in the plasma physics involved.

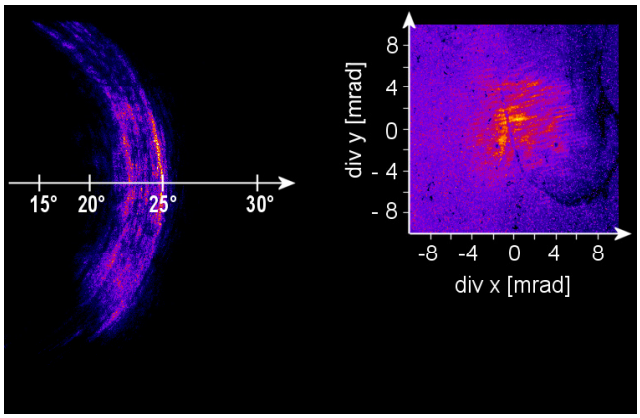

(a)

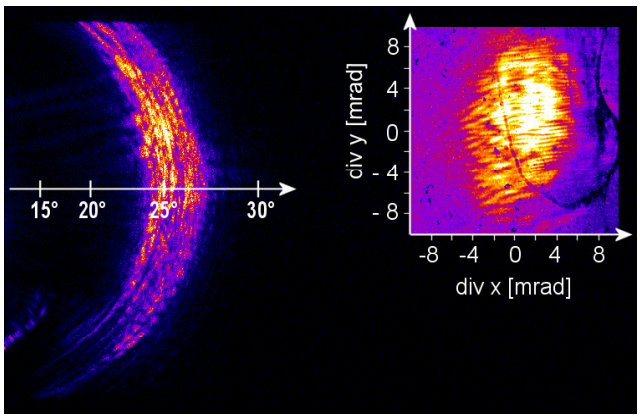

(b)

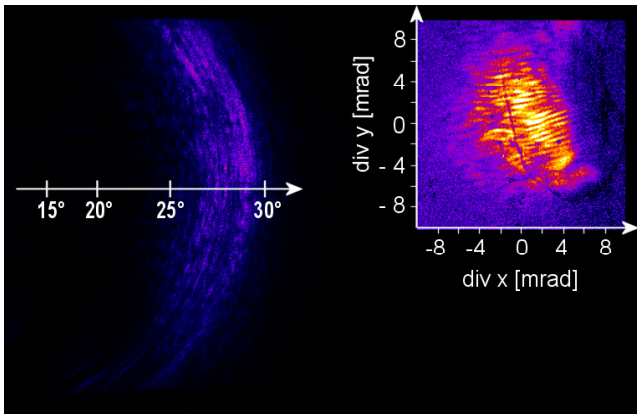

(c)

Figure 38: Images of the refracted main pulse beam for several shots of the last Zr beamtime during which also the scans discussed in the previous chapters were done with the GRIP angles of 25 (a), 27 (b) and 31.5 (c) degrees. The insets show the respective XRL footprints taken at the same time.

4.2.7 *Plasma spectroscopy*

The plasma spectrometer was employed to analyze the emission between 1.5 and 5 nm under an angle of view of roughly 45° to the target surface. This spectral region is of interest since it is the energetic range of the emissions of the 4f-3d and 4p-3d transitions of nickel-like and higher ionized species of the employed target materials. While the 4f level is energetically very close to the 4d level which is the upper level of the XRL transition (see figure 39), the 4p level is the lower XRL transition level, and all three transitions are correlated in intensity [63].

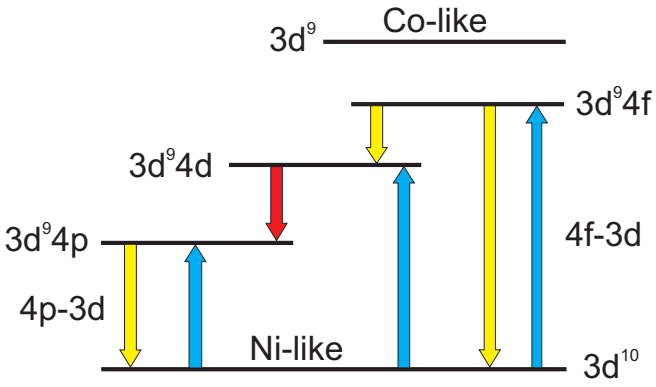

Figure 39: Energy level and transition scheme for a Ni-like ion. The lower laser level $3d^9 4p$, the upper laser level $3d^9 4d$ and the neighboring level $3d^9 4f$ are populated by electronic collisional excitation, so the transitions marked in yellow also take place and were analyzed by the plasma spectrometer.

In figure 40, a typical spectrum of a Pd XRL plasma is shown. The lines have been identified to belong to the respective ionization states by gauging the spectrum with a thin Cr filter, having an absorption edge at 2.16 nm [65] and comparison to the spectral data available in [66].

As can be seen, the Ni-like and Co-like emission lines are dominant, which can be explained by the fact that the spectrometer is integrating over the entire plasma length as well as over the entire emission time. At least after the fast heating process to achieve the population inversion, the slower process of higher ionization is bound to follow, so an over-ionization can well take place with the energy still available in the relaxing plasma (see also [64]). This is supported by the Zr XRL plasma spectrum depicted in figure 41, taken from a shot with the optimal conditions as found in chapter 4.2.3.

Even at only 1/4 of total pumping energy, the higher charge states are dominating, pointing towards a potential for a substantial decrease in the pumping energy as shown in the next chapter.

Figure 42 shows a series of spectra taken with the Zr XRL at a GRIP angle of 27° from the same shots that were analyzed in figure 27 for

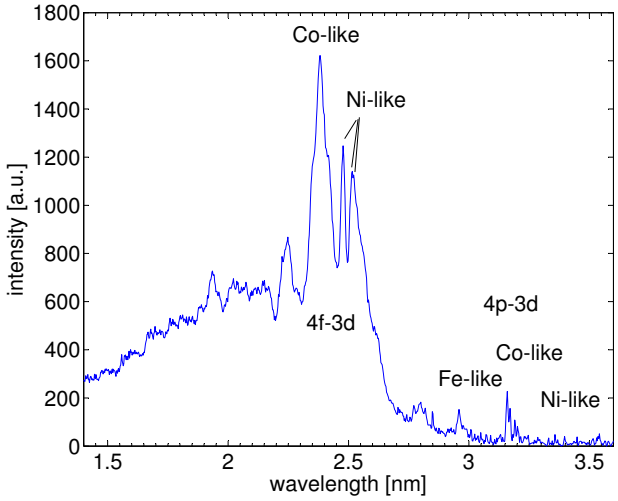

Figure 40: Plasma emission of a Pd XRL, taken at 5 J preamplifier energy [64].

different delays between long and short pulse.

The surprising feature is the minimum of the Ni-like peak height around the delay values which were found optimal for the XRL performance (roughly 400 ps). This can be taken as an indication that the abundance of Ni-like ions not necessarily results in a good XRL operation since the spectrometer gives spectra which are integrated in space and time. The optimal condition for lasing requires a high degree of Ni-like population in the very small active area, and is specifically also sensitive to over-ionization. The detailed analysis of the ionic plasma situation

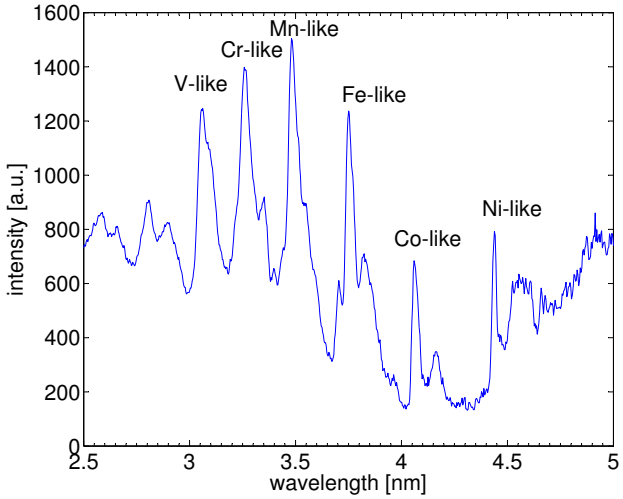

Figure 41: Plasma emission spectrum of a Zr XRL, taken at 1.2 J preamplifier energy.

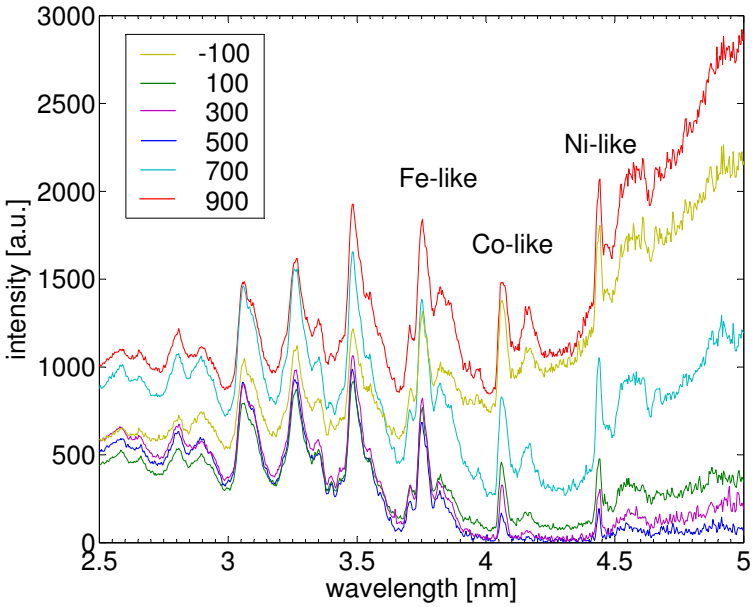

Figure 42: Plasma emission spectra of a Zr XRL for the optimal GRIP angle at 1.2 J preamplifier energy for different delays between long and short pulse in picoseconds. The optimal delay for the XRL performance was found to be 400 ps.

therefore requires a study also of the time dependence of the plasma. On the other hand, the overall background towards longer wavelengths is lowest for the optimal XRL delay region, which can be explained in such a way that there, the energy is used specifically for pumping the inversion and not for an overall heating of the plasma. This feature therefore represents a signature for efficient pumping of the laser plasma, which is easily identified for an on-line optimization, which will be very helpful in future XRL experiments with the PHELIX main amplifier due to the limited number of available shots.

4.2.8 *Pumping energy optimization with Zr and Pd*

A very important figure of merit for the practicability of an XRL is the lowest pump energy at which stable lasing can be accomplished. Although the achieved XRL output energies are also important, a lowering of the required pumping laser energy usually opens the field for an increasing number of users since the abundance of available laser systems around the world increases strongly with a reduction of the energy specifications. This is also linked to the repetition rate at which experiments can be performed: the lower the output energy of a laser system, the higher is its achievable repetition rate.

Figure 43 shows the results of a dedicated Zr shot series to determine

the lowest pumping laser energy requirements under the optimal conditions as found in the experiment described in chapter 4.2.3 with a target length of 5.1 mm.

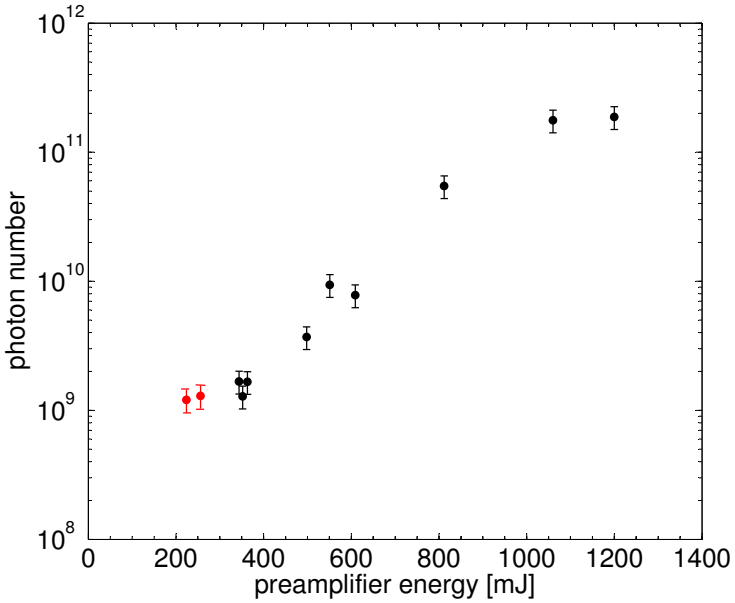

Figure 43: Scan of the pumping laser energy with a 5.1 mm long Zr target under optimal delay and GRIP angle conditions. The two shots marked in red were taken with a narrower focused prepulse line.

At the lower end, the limit could be pushed further down by decreasing the prepulse line width to about 60 µm (as compared to 90 µm for the other shots), although this made the system more susceptible to fluctuations in the overlap of the focal lines. As can be seen, the limit is around 250 mJ, which, mostly due to losses in the compressor, corresponds to a total energy on target of roughly 170 mJ.

Earlier experiments with a Pd XRL on the PHELIX setup, performed at very high GRIP angles around 45° indicated the necessity of pumping energies of at least 4 J. This rendered this lasing element rather unattractive because of the need to use the 45 mm head of the preamplifier which limited the repetition rate to once every 15 min (which, due to improvements of the overall wavefront performance could recently be lowered to once every 12 min).

Here, the optimization results with Zr motivated a new attempt with a 6.5 mm long Pd target under three different GRIP angles and delays similar to the ones from the Zr optimization. The results shown in figure 44 point to a lower threshold at about 1 J preamplifier energy, which corresponds to less than 700 mJ energy on target. Again, a tighter focusing of the prepulse resulted in a lowering of the threshold. Furthermore, a full preamplifier shot taken under these conditions yielded a photon

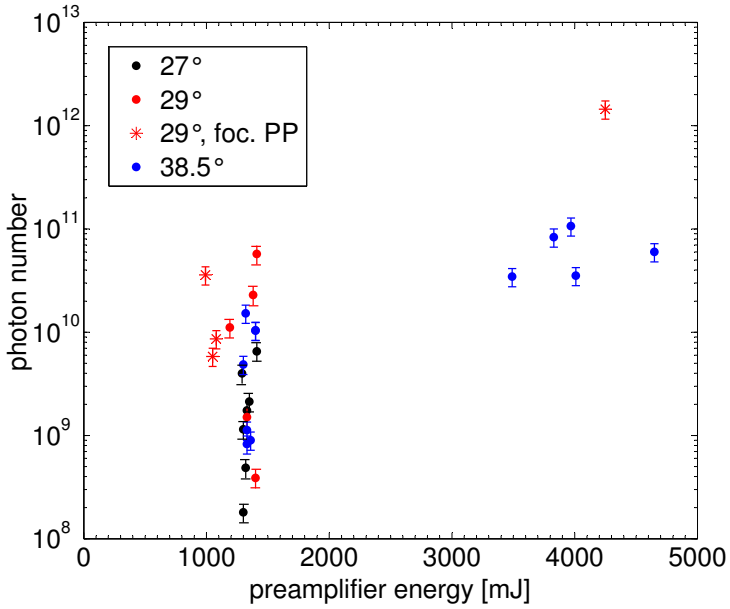

Figure 44: Scan of the pumping laser energy with a 6.5 mm long Pd target with delays of 200-400 ps and three different GRIP angles. The 29° points marked with an asterisk (*) were taken with a prepulse which was focused more tightly.

number of 1.5×10^{12} photons which, at a photon energy of 84.3 eV, equals to a pulse energy of 20 µJ.

5 SPECTROSCOPY SETUP

5.1 SCIENTIFIC MOTIVATION

The driving idea behind the XRL development at GSI is the need for a short-wavelength radiation source for spectroscopy on Li-like heavy ions in a storage ring [67]. Laser spectroscopy of radioactive isotopes and of highly-charged heavy ions as such has been one of the major domains of research at GSI, and many experiments using optical lasers as excitation sources or means of cooling the stored ion bunches have been performed (see, e.g., [68] [69] [70]). Such experiments have also yielded important information about nuclear properties like nuclear spins, moments and charge radii (see, e.g., [71]). Spectroscopy of neutral atoms and singly charged ions generally are the prime source of information on ground-state properties of short-lived radio-isotopes [72] [73].

However, when going to high charge states of the ions, the transition energies become so large that optical lasers, even with the use of the Doppler shift of nearly relativistic particles, are not able to provide the excitation energies without employing special techniques like multi-photon processes. Figure 45 shows the transition energies for the 2s1/2-2p1/2 transitions of Li-like heavy ions.

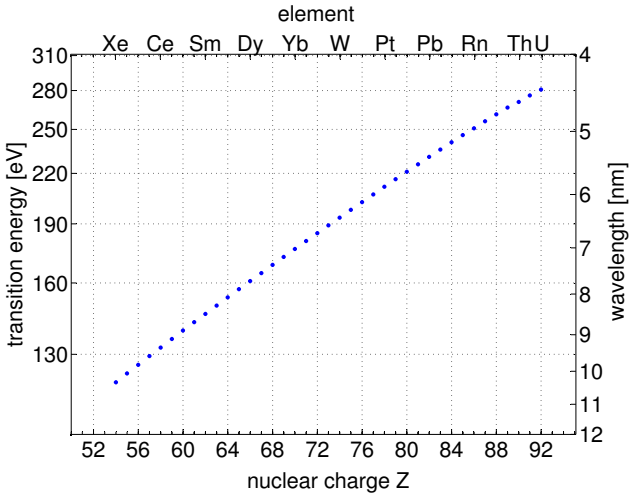

Figure 45: Energies and wavelengths for the 2s1/2-2p1/2 transitions of Li-like ions [74].

This charge state is interesting because the systems with three electrons are still accessible to precise calculations while the transition energies

are still below 0.5 keV. The precise measurement of these energies for different isotopes of one element can provide interesting information about nuclear charge radii and can be used as test for QED calculations.

As can be seen, the range of 100 to 300 eV for the upper part of the periodic table is significantly higher than the photon energies of the XRLs described here (Ag XRL: 89 eV), but this can be bridged easily by making use of the Doppler shift which is present in the case of counterpropagation of the XRL and the relativistic ion beams. Moreover, this technique is enabling the spectroscopy with a fixed-frequency laser source in the first place, since the photon energy the ions "see" can be tuned by a fine variation of the ion velocity which can be achieved by tuning the voltage of the ESR's electron cooler.

The necessary ion velocities are shown in figure 46 together with the technical constraints of the ESR in its present state.

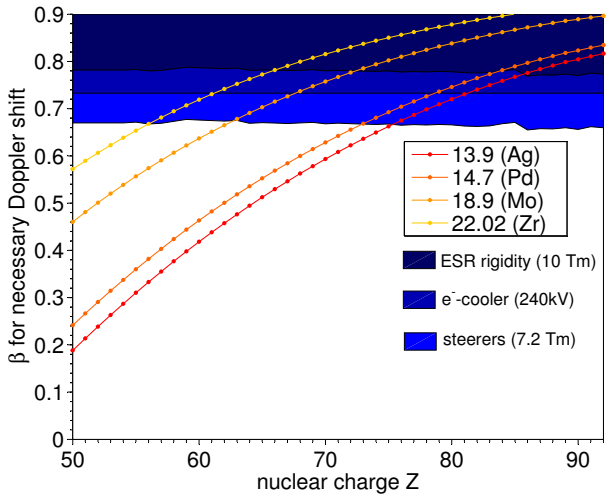

Figure 46: Required ion velocities in units of c to excite the 2s1/2-2p1/2 transitions of Li-like ions of a given nuclear charge with a given (fixed) laser wavelength in nanometers, together with limits imposed by critical components in the storage ring.

Even at the longest XRL wavelength of 22.02 nm, several elements with $Z \leq 56$ (Ba), including Xenon which is used rather frequently at GSI, are accessible, while the Pd XRL with 14.7 nm can reach up to $Z \leq 72$ which is Li-like Hafnium.

5.2 EXPERIMENTAL SCHEME

Due to the short lifetimes of the excited 2p1/2 state of the heavier elements in the range of 70 to 200 ps, the experiment does not necessarily

have to be carried out in the storage ring itself, but can rather be set up in an adjacent beamline which was originally constructed to re-inject cooled ions from the ESR back into the synchrotron, the so-called reinjection channel (see figure 47).

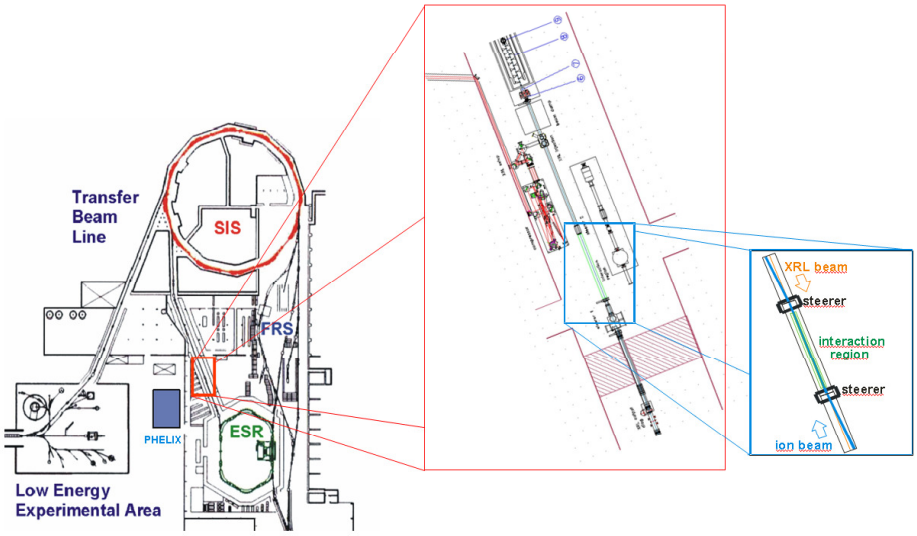

Figure 47: Overview of the experimental surroundings at GSI with closer views of the setup.

This has the practical advantage that the vacuum requirements are orders of magnitude weaker (around 10^{-7} mbar) than in the ring itself and besides makes the preparations independent of other experiments using the ESR. In the recent past, the same location is occupied by the HITRAP facility [75], but arrangements have been made to share the experimental area without the need for major changes.

An experiment to measure the isotope shift will then start with the filling of the ESR with the desired isotope species, which by accumulation of several synchrotron cycles can reach an amount of more than 10^8 ions. The stored ion beam will then be cooled by the electron cooler to a momentum distribution $\Delta p/p$ which according to [76] is dependent on the number of stored ions N:

$$\frac{\Delta p}{p} = 6.8 \times 10^{-7} \times N^{0.27}, \tag{5.1}$$

resulting in $\Delta p/p \approx 10^{-4}$ for 10^8 stored ions. This broadening allows for an easy start of the scan and should provide a strong resonance signal which can then be lowered by decreasing the ion beam intensity to 10^7, resulting in $\Delta p/p \approx 5 \times 10^{-5}$. After sufficient cooling and the spacial concentration in an ion bunch of a few meters length, the ions are extracted synchronously with the firing of the PHELIX amplifier

system in such a way that the XRL pulse will coincide with the counterpropagating ion bunch in the interaction region also shown in figure 47. Here, also the detection system for the de-excitation fluorescence radiation (which is Doppler shifted once more) is located, consisting either of photomultiplier-based scintillation detectors or an array of semiconductor diodes. Utilizing mainly the photons emitted in the direction of the ion beam, the energy is again increased by a factor of two, as compared to the XRL radiation used for the excitation. To achieve the best possible overlap between the two beams, two magnetic steerers will bend the ion beam into a slight "Z" shape so that a few meters away from the steerers, two multilayer mirrors can be mounted in the beamline to send the XRL beam parallel to the ion beam in the overlap region. To protect the downstream parts of the HITRAP facility, the ion beam is then guided onto a beam dump.

A second isotope can then be treated the same way, and it should be possible to determine the resonances with a few hundred shots, so a few days of beamtime should be sufficient.

With regard to the requirements for the XRL as an excitation source, an extensive study [20] has shown that the values reached in earlier XRL experiments are broadly sufficient. The bandwidth of the XRL could not be determined precisely with the PHELIX setup due to the resolution of the employed spectrometer in the range of 10^{-3}, but other experiments have shown that the XRL bandwidth can be expected to be around 4×10^{-5} [77], which is comparable to the momentum distribution of the ions. From the Einstein A coefficients and oscillator strengths tabulated in [78], an interaction cross section of 10^{-16} /cm² can be estimated via equation 2.14, which is rather small due to the small spectral overlap with the natural transition bandwidths which is only $\Delta\lambda_{nat}/\lambda \approx 10^{-7}$. Considering the geometrical conditions, the probability for the excitation of an ion with an XRL pulse energy of 10 µJ can be estimated to be in the range of $P_{ex} = 1$ to 3×10^{-4}, which, at a number of 10^8 ions per bunch should provide a reasonably strong signal.

Since with the given magnetic focusing system at the reinjection channel, the ion beam can be collimated to a width of several millimeters over a distance of several meters, also the XRL beam should ideally have the same proportions. To achieve a collimated beam over a long distance, a spherical multilayer mirror can be used, positioned in such a way that its focus is in the exit plane of the XRL, tilted by a small angle (some degrees) which allows the collimated beam to pass the target in a distance of some centimeters. The beam diameter d at a distance $L \gg f$ after a focusing element can be estimated from the source size s and the divergence δ of the XRL to be

$$d = \sqrt{L \times s \times \delta}. \tag{5.2}$$

The source size of the PHELIX XRL has not been measured yet, but it

should be similar to the measurements at LLC (see chapter 4.1.1) which yielded an approximate source size s of $25 \times 40\ \mu m^2$. An analysis of the footprint images taken with the PHELIX setup (see, e.g., insets in 37) leads to a divergence of 7×9 mrad in the horizontal and the vertical directions, respectively. Assuming an overall XRL beam path of 8 m, the XRL beam FWHM cross section will be $1.2 \times 1.7\ mm^2$ which matches the dimensions of the ion beam very well.

6 DISCUSSION AND CONCLUSIONS

During this thesis, major improvements of the performance of plasma based XRLs in the wavelength range below 20 nm have been achieved, due to a systematic study of the influence of the angle of incidence, delay between pre- and main pulse, and the focusing of the pump pulses in the GRIP scheme. New diagnostics in the form of a high-resolution keV plasma position sensor and a system to image the refracted pump laser light have been developed and tested successfully, providing important input for theoretical work on which approaches for further improvement can be based. In the case of the plasma spectrometer, the pumping energy required for a clear signal has been reduced significantly and the feasibility of a relation between the spectra and the abundances of certain ionic species has been shown in [64].

A systematic optimization, based on the experimental evidence from a joint European experimental campaign, lead to a considerable improvement of the XRL performance and especially an increase of the repetition rate for an XRL with a wavelength below 15 nm. This necessitated the introduction of a system of computer-controlled optomechanics, reference points and diagnostics for reproducible and user-independent alignment and an overall improvement in mechanical stability.

As a result, the development of the PHELIX XRL from an experimental stage with days of preceding preparation to a reliable and reproducible light source has been accomplished. In addition, key parameters were identified for a renewed experimental effort to approach the so-called "water-window", i.e. XRL wavelengths around 5 nm, with still moderate pump energies around or even below 100 J. To reach this wavelength range, situated below the absorption edge of oxygen, is an important prerequisite for the use of such a system in bio-medical research. A proposal for an experimental campaign at PHELIX was accepted by an international referee board of the EU Integrated Infrastructure Initiative "Laserlab Europe".

GRIP ANGLE OPTIMIZATIONS Figure 48 shows the scaled energies achieved in the Mo and Zr XRL experiments with GRIP angles scaled to a pump laser wavelength (see eq. 4.2) of 1054 nm. Both XRLs reach their best performance around a GRIP angle value of 26° with similar peak output energies, although one would have expected an increase of the optimal GRIP angle for heavier lasing elements (when going from $Z = 40$ for Zr to $Z = 42$ for Mo), which is supported by the Pd XRL ($Z = 46$) which showed a better performance at 29° than at 27° or 38.5°. The reason

for this deviation might be the different long pulse conditions (300 ps for Mo vs. 800 ps for Zr) which complicates a direct comparison of the two cases. In a Pd XRL with 120 ps long pulse duration [60], an optimum angle (again, scaled to 1054 nm) of roughly 27.5° has been reported. As has already been mentioned, the dependency of the optimal GRIP angle on the electron density is rather strong (10% change of density results in an angular change of 1.5°), and so even the theoretical prediction of a GRIP angle of 26.5° for an Ag XRL ($Z = 47$) [43] can still be seen as a good agreement.

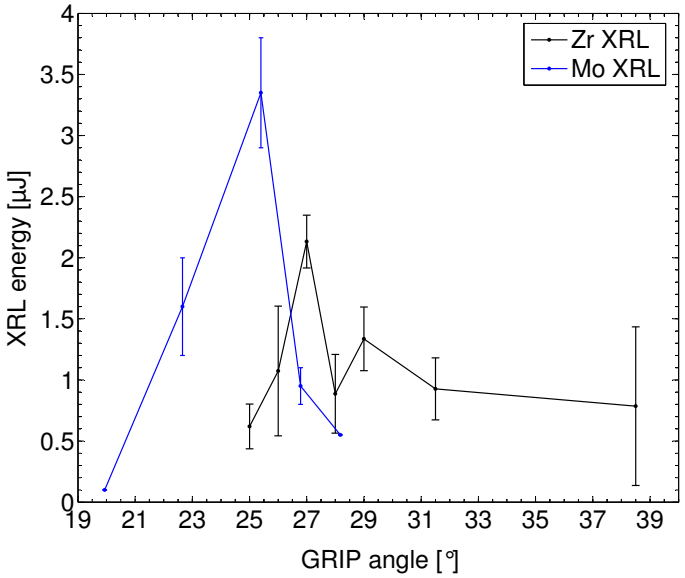

Figure 48: XRL output energies of the Mo XRL at LLC and the Zr XRL at PHELIX with GRIP angles scaled to the PHELIX laser wavelength.

PUMPING ENERGY OPTIMIZATION The lowest energy values on target for Zr and Pd with the PHELIX setup were 170 µJ and 680 µJ, respectively. Keenan et al. [17] have reported a threshold value of 150 µJ with a Ti:Sa-based system for a Mo XRL which to date is still seen as the lowest reported value, so a Zr XRL with roughly the same pumping energy requirements can be regarded as competitive. A simulation based on the RADEX code for a Ti:Sa GRIP system with a GRIP angle of 20° (see [60]) yielded total energies in excess of roughly 1.3 J as necessary for strong lasing, so an energy threshold value of roughly half this value is a good success. Even with the PHELIX system in its current state, total pump energies 1 J on target are available every 4 min, which, as has been mentioned before, could be reduced by optimization to almost 1 shot/min in the near future.

BEAM QUALITY Although an optimization of the divergence values for the Zr XRL, shown to be around 6-9 mrad (similar for the Pd XRL) has not been performed in a dedicated beamtime, these values have already been proven to be sufficient for the envisaged application as an excitation source for heavy-ion spectroscopy. The source size can be expected to be rather small (25-40 µm) and the overall divergence is low enough to still fit on standard 1"-sized multilayer collimation optics even after meters of propagation which should allow for reasonably long beam transport distances and focusing characteristics. The deviation from the target axis, originating in refraction of the XRL beam in the plasma and measured to be less than 2 mrad for the Zr XRL (again, similar for the Pd XRL) compares rather well to values of 3.6 mrad reported for a Mo XRL by Keenan et al [17]. Such a low value can be seen as an additional proof of the GRIP scheme, since this means that the XRL is traveling through a region of small density gradients at electron densities still producing strong gain.

The strong modulations in the beam profile have been shown to be due to a lack of spatial coherence [56], which is a typical feature of TCE-based XRLs. A way to greatly improve this feature is to change from the ASE scheme to an oscillator-amplifier scheme by seeding the plasma with the injection of an x-ray pulse produced by high harmonic generation, which has been shown to be very beneficial for the XRL beam quality [79]. Currently, a project in cooperation with a group at University of Würzburg specialized on highest harmonic generation in gas targets (see, e.g., [4]) is making good progress at the PHELIX setup with a prospect of achieving the necessary order of harmonics for seeding the PHELIX XRL even at the comparably long pulse durations available here.

All of the above-mentioned aspects and improvements show that the PHELIX XRL system already meets the requirements for first applications, and ongoing efforts will make it an even more versatile tool in the near future.

7 OUTLOOK

XRL DEVELOPMENT Current and near-term work is focused on two approaches. On the one hand, as has already been mentioned, a joint effort is underway to implement the concept of seeding based on HHG in gas targets which has been proven to be very beneficial for the XRL beam quality, especially the beam profile. On the other hand, with the availability of the PHELIX main amplifier beam, the preparations for a series of experiments with the aim of extending the XRL wavelength range below 10 nm and possibly into the so-called water window (2.3–4.3 nm), interesting for biological investigations have started and a first beamtime is expected still in 2007 (Laserlab Europe Proposal 2006/P008).

The diagnostics presented in this work, together with the input from recently started theoretical approaches will be specifically useful in this effort since the required amounts pumping energy are difficult to predict. Additional informations about the achieved plasma conditions (e.g., the reached charge states) are needed to ensure the best possible progress even at the comparably limited amount of shots available with the main amplifier.

APPLICATIONS First applications of XRL systems with higher repetition rate, but otherwise very similar to the PHELIX XRL have been demonstrated recently. These range from plasma interferometry (see, e.g., [80]) where the short-wavelength, high-brilliance aspect allowed the probing of dense plasmas, to XRL-based microscopy [81], reaching a resolution below 38 nm.

The rare abundance of well-defined radiation sources in this wavelength regime makes the XRLs attractive as calibration sources of XUV detectors. Figure 49 shows the beam profile of the Zr XRL recorded with an image plate developed for medical imaging which is foreseen to be used as an imaging medium for plasma physics experiments.

The mounting of the already delivered last beamline parts for the transport of the PHELIX preamplifier beam (see figure 50) will make the XRL available in GSI's reinjection channel (see 5.2) for first tests of synchronization with the accelerator early 2008.

From the current point of view, plasma-based XRLs have reached the status of actually usable devices which, due their infrastructural requirements scaled down from storehouse-sized facilities to table-top size, are attractive also for university-scale laboratories [82].

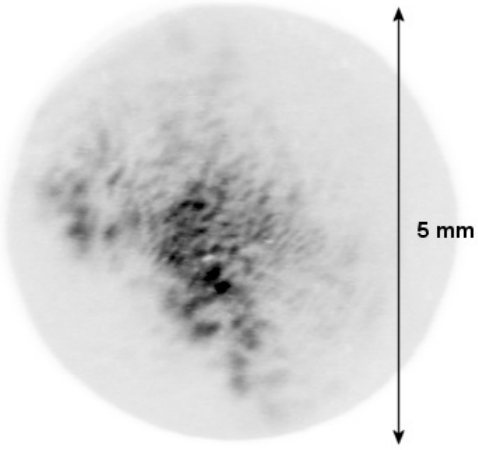

Figure 49: Image plate record of a footprint of the PHELIX Zr XRL, taken in the same beamtime as the footprints in figure 34. Image courtesy of A. Otten, GSI plasma physics department.

Figure 50: Transport beamline across the PHELIX laserbay towards the reinjection channel.

BIBLIOGRAPHY

[1] W. Ackermann et al., 'Operation of a free-electron laser from the extreme ultraviolet to the water window', *Nature Photonics*, vol. 1, p. 336, 2007. (Cited on page 2.)

[2] G. Schriever, K. Bergmann and R. Lebert, 'Narrowband laser produced extreme ultraviolet sources adapted to silicon/molybdenum multilayer optics', *J. Appl. Phys.*, vol. 83, p. 4566, 1998. (Cited on page 2.)

[3] U. Stamm, H. Schwoerer and R. Lebert, 'Strahlungsquellen für die EUV-Lithographie', *Physik Journal*, vol. 1, p. 33, 2002. (Cited on page 2.)

[4] J. Seres, E. Seres, A. J. Verhoef, G. Tempea, C. Streli, P. Wobrauschek, V. Yakovlev, A. Scrinzi, C. Spielmann and F. Krausz, 'Laser technology: Source of coherent kiloelectronvolt X-rays', *Nature*, vol. 433, p. 596, 2005. (Cited on pages 2 and 59.)

[5] J.-F. Hergott, 'Extreme-ultraviolet high-order harmonic pulses in the microjoule range', *Phys. Rev. A*, vol. 66, p. 021801, 2002. (Cited on page 2.)

[6] Y. Kato, H. Daido, R. Kodama, K. Murai, G. Yuan, M. S. Schulz, M. Yamanaka, M. Takagi, T. Kanabe, S. Nakai, D. Neely, A. G. MacPhee, C. L. S. Lewis, G. E. Slark, M. Niibe, M. Tsukamoto, Y. Fukuda, H. Tsunemi, S. Nomoto, I. Kodama, T. Honda, K. Shinohara, H. Iwasaki and T. Yoshinobu, 'Recent progress in collisionally excited x-ray laser research at the Institute of Laser Engineering', in S. Suckewer (editor), 'SPIE proceedings', vol. 2012, pp. 12–21, SPIE, 1994. (Cited on pages 3 and 8.)

[7] T. Mocek, B. Rus, A. R. Präg, M. Kozlová, G. Jamelot, A. Carillon and D. Ros, 'Beam properties of a deeply saturated, half-cavity zinc soft-x-ray laser', *J. Opt. Soc. Am. B*, vol. 20(6), p. 1386, 2003. (Cited on pages 3 and 8.)

[8] D. L. Matthews, P. L. Hagelstein, M. D. Rosen, M. J. Eckart, N. M. Ceglio, A. U. Hazi, H. Medecki, B. J. MacGowan, J. E. Trebes, B. L. Whitten, E. M. Campbell, C. W. Hatcher, A. M. Hawryluk, R. L. Kauffman, L. D. Pleasance, G. Rambach, J. H. Scofield, G. Stone and T. A. Weaver, 'Demonstration of a Soft X-Ray Amplifier', *Phys. Rev. Lett.*, vol. 54(2), p. 110, 1985. (Cited on pages 3 and 11.)

[9] T. N. Lee, E. A. McLean and R. C. Elton, 'Soft x-ray lasing in neonlike germanium and copper plasmas', *Phys. Rev. Lett.*, vol. 59(11), p. 1185, 1987. (Cited on page 3.)

[10] J. Nilsen and J. C. Moreno, 'Nearly Monochromatic Lasing at 182 angstrom in Neonlike Selenium', *Phys. Rev. Lett.*, vol. 74(17), p. 3376, 1995. (Cited on page 3.)

[11] H. Daido, R. Kodama, K. Murai, G. Yuan, M. Takagi, Y. Kato, I. W. Choi and C. H. Nam, 'Significant improvement in the efficiency and brightness of the J=0-1 19.6-nm line of the germanium laser by use of double-pulse pumping', *Opt. Lett.*, vol. 20(1), p. 61, 1995. (Cited on page 3.)

[12] P. V. Nickles, V. N. Shlyaptsev, M. Kalachnikov, M. Schnürer, I. Will and W. Sandner, 'Short Pulse X-Ray Laser at 32.6 nm Based on Transient Gain in Ne-like Titanium', *Phys. Rev. Lett*, vol. 78, p. 2748, 1997. (Cited on pages 3 and 12.)

[13] J. Dunn, Y. Li, A. L. Osterheld, J. Nilsen, J. R. Hunter and V. N. Shlyaptsev, 'Gain Saturation Regime for Laser-Driven Tabletop, Transient Ni-Like Ion X-Ray Lasers', *Phys. Rev. Lett.*, vol. 84, p. 4834, 2000. (Cited on page 3.)

[14] P. Neumayer, W. Seelig, K. Cassou, A. Klisnick, D. Ros, D. Ursescu, T. Kuehl, S. Borneis, E. Gaul, W. Geithner, C. Haefner and P. Wiewior, 'Transient collisionally excited X-ray laser in nickel-like zirconium pumped with the PHELIX laser facility', *Applied Physics B: Lasers and Optics*, vol. 78(7), p. 957, 2004. (Cited on page 3.)

[15] D. Ros, A. Klisnick, D. Joyeux, D. Phalippou, O. Guilbaud, J. Kuba, A. Carillon, G. Jamelot, R. Smith, M. Edwards, F. Strati, G. J. Tallents, H. Daido, H. Tang, P. Neumeyer, D. Urescu, T. Kuhl, J.-C. Chanteloup and K. Bouhouch, 'Recent Progress on the Understanding of the Transient Ni-like Ag X-ray Laser at 13.9 nm at LULI facilities', in 'AIP Conf. Proc.', vol. 641, pp. 69–76, AIP, Aspen, Colorado (USA), 2002. (Cited on page 3.)

[16] A. Klisnick, G. Jamelot, D. Ros, A. Carillon, P. Jaegle, M. Boussoukaya, O. Guilbaud, J. Kuba, R. Smith, J.-C. Lagron, L. Vanbostal, D. Joyeux, D. Phalippou, S. Sebban, A. Touati, M. A. H. d. Penhoat, F. Ballester, E.-J. Petit, B. Rus, T. Mocek, F. Strati, M. Edwards, G. J. Tallents, R. Keenan, S. Topping, C. L. S. Lewis, P. Neumeyer, D. Ursescu, T. Kühl, H. Tang and H. Daido, 'Development and applications of x-ray lasers at LSAI/LIXAM', in 'AIP Conf. Proc.', vol. 641, pp. 166–173, AIP, Aspen, Colorado (USA), 2002. (Cited on page 3.)

[17] R. Keenan, J. Dunn, P. K. Patel, D. F. Price, R. F. Smith and V. N. Shlyaptsev, 'High-Repetition-Rate Grazing-Incidence Pumped X-Ray

Laser Operating at 18.9 nm', *Phys. Rev. Lett.*, vol. 94(10), p. 103901, 2005. (Cited on pages 3, 58, and 59.)

[18] B. M. Luther, Y. Wang, M. A. Larotonda, D. Alessi, M. Berrill, M. C. Marconi, J. J. Rocca and V. N. Shlyaptsev, 'Saturated high-repetition-rate 18.9-nm tabletop laser in nickel-like molybdenum', *Opt. Lett.*, vol. 30(2), p. 165, 2005. (Cited on page 3.)

[19] S. Eliezer, *The interaction of high-power lasers with plasmas*, IOP Publishing Ltd., 2002. (Cited on pages 5 and 13.)

[20] P. Neumayer, *Ein transienter Röntgenlaser zur Laserspektroskopie an Lithium-ähnlichen Ionen*, Ph.D. thesis, Technische Universität Darmstadt, 2003. (Cited on pages 6, 13, 18, 24, 38, 43, and 54.)

[21] McWhirter, *Plasma Diagnostic Techniques*, New York: Academic, 1965. (Cited on page 6.)

[22] H. R. Griem, *Principles of Plasma Spectroscopy*, Cambridge Monographs on Plasma Physics, 1997. (Cited on page 6.)

[23] D. Colombant and G. F. Tonon, 'X-ray emission in laser-produced plasmas', *Journal of Applied Physics*, vol. 44(8), p. 3524, 1973. (Cited on pages 7 and 12.)

[24] A. Einstein, 'Zur Quantentheorie der Strahlung', *Phys. Z.*, vol. 18, p. 121, 1917. (Cited on page 7.)

[25] W. Seelig, 'High Power Gas Lasers', *SPIE Proceedings*, vol. 455, p. 2, 1984. (Cited on page 8.)

[26] G. Linford, E. Peressini, W. Sooy and M. Spaeth, 'Very long lasers', *Applied Optics*, vol. 13(2), p. 379, 1974. (Cited on page 9.)

[27] G. J. Tallents, 'The physics of soft x-ray lasers pumped by electron collisions in laser plasmas', *Journal of Physics D: Applied Physics*, vol. 36(15), p. R259, 2003. (Cited on pages 9, 11, and 40.)

[28] R. A. London, 'Beam optics of exploding foil plasma x-ray lasers', *Physics of Fluids*, vol. 31(1), p. 184, 1988. (Cited on page 10.)

[29] M. Born and E. Wolf, *Principles of Optics*, chap. Foundations of geometrical optics, p. 116, Cambridge University Press, 1999. (Cited on page 10.)

[30] G. J. Pert, 'Refraction and absorption in plasma atmospheres', *Plasma Physics*, vol. 25(4), p. 387, 1983. (Cited on page 10.)

[31] J. A. Plowes, G. J. Pert, S. B. Healy and D. T. Toft, 'Beam modelling for x-ray lasers', *Optical and Quantum Electronics*, vol. 28(3), p. 219, 1996. (Cited on page 10.)

[32] J. G. Lunney, 'Waveguiding in soft x-ray laser experiments', *Applied Physics Letters*, vol. 48(14), p. 891, 1986. (Cited on page 10.)

[33] C. L. S. Lewis, D. Neely, D. M. O'Neill, J. O. Uhomoibhi, M. H. Key, Y. A. Hadithi, G. J. Tallents and S. A. Ramsden, 'An injector/amplifier double target configuration for the Ni-like Ge X-ray laser scheme', *Opt. Commun.*, vol. 91, p. 71, 1992. (Cited on page 11.)

[34] J. Zhang, A. B. MacPhee, J. Lin, E. Wolfrum, R. Smith, C. Danson, M. H. Key, C. L. S. Lewis, D. Neely, J. Nilsen, G. J. Pert, H. J. Tallents and J. S. Wark, 'A Saturated X-ray Laser Beam at 7 Nanometers', *Science*, vol. 276, p. 1097, 1997. (Cited on page 11.)

[35] H. Daido, 'Review of soft x-ray laser researches and developments', *Reports on Progress in Physics*, vol. 65(10), p. 1513, 2002. (Cited on pages 11 and 40.)

[36] R. C. Elton, *X-Ray Lasers*, Academic Press, Inc., San Diego, CA, USA, 1990. (Cited on page 11.)

[37] R. C. Elton, 'Extension of 3p -> 3s ion lasers into the vacuum ultraviolet region', *Appl. Opt.*, vol. 14(1), p. 97, 1975. (Cited on page 11.)

[38] A. V. Vinogradov, I. Y. Skobelev, I. I. Sobel'man and E. A. Yukov, 'Population-inverted medium for stimulated emission in vacuum ultraviolet', *Sov. J. Quantum Electron.*, vol. 5, p. 1192, 1975. (Cited on page 11.)

[39] Y. V. Afanas'ev and V. N. Shlyaptsev, 'Formation of a population inversion of transitions in Ne-like ions in steady-state and transient plasmas', *Sov. J. Quantum Electron.*, vol. 19, p. 1606, 1989. (Cited on page 12.)

[40] J. Collier, D. Pepler, C. Danson, J. Warwick, C. Lewis and D. Neely, in 'RAL Ann. Rep. 209', , 1996. (Cited on page 12.)

[41] T. Kawachi, M. Kado, M. Tanaka, A. Sasaki, N. Hasegawa, A. V. Kilpio, S. Namba, K. Nagashima, P. Lu, K. Takahashi, H. Tang, R. Tai, M. Kishimoto, M. Koike, H. Daido and Y. Kato, 'Gain saturation of nickel-like silver and tin x-ray lasers by use of a tabletop pumping laser system', *Phys. Rev. A*, vol. 66(3), p. 033815, 2002. (Cited on page 12.)

[42] G. J. Pert, 'The hybrid model and its application for studying free expansion', *Fluid Mech.*, vol. 131(1), p. 401, 1983. (Cited on page 13.)

[43] G. J. Pert, 'Optimizing the performance of nickel-like collisionally pumped x-ray lasers', *Physical Review A (Atomic, Molecular, and Optical Physics)*, vol. 73(3), 033809, 2006. (Cited on pages 14 and 58.)

[44] T. Kühl, R. Bock, S. Borneis, E. Brambrink, H. Brand, J. Caird, E. Campbell, K. Cassou, E. Gaul, S. Goette, C. Haefner, T. Hahn, H. Heuck, D. Hoffmann, D. Javarkova, A. Klisnick, H.-J. Kluge, S. Kunzer, T. Merz, P. Neumayer, P. Nickles, M. Perry, D. Reemts, D. Ros, M. Roth, S. Samek, W. Sandner, G. Schaumann, F. Schrader, W. Seelig, A. Tauschwitz, R. Thiel, D. Ursescu, P. Wiewior, U. Wittrock and B. Zielbauer, 'PHELIX - Status and First Experiments', *Hyperfine Interactions*, vol. 162(1), p. 55, 2005. (Cited on page 15.)

[45] P. Neumayer, R. Bock, S. Borneis, E. Brambrink, H. Brand, J. Caird, E. Campbell, E. Gaul, S. Goette, C. Haefner, T. Hahn, H. Heuck, D. Hoffmann, D. Javorkova, H.-J. Kluge, T. Kuehl, S. Kunzer, T. Merz, E. Onkels, M. Perry, D. Reemts, M. Roth, S. Samek, G. Schaumann, F. Schrader, W. Seelig, A. Tauschwitz, R. Thiel, D. Ursescu, P. Wiewior, U. Wittrock and B. Zielbauer, 'Status of PHELIX laser and first experiments', *Laser and Particle Beams*, vol. 23, p. 385, 2005. (Cited on page 15.)

[46] D. Strickland and G. Mourou, 'Compression of amplified chirped optical pulses', *Opt. Commun.*, vol. 56, p. 219, 1985. (Cited on page 15.)

[47] G. Cheriaux, P. Rousseau, F. Salin, J. P. Chambaret, B. Walker and L. F. Dimauro, 'Aberration-free stretcher design for ultrashort-pulse amplification', *Opt. Lett.*, vol. 21(6), p. 414, 1996. (Cited on page 15.)

[48] M. D. Perry, D. Pennington, B. C. Stuart, G. Tietbohl, J. A. Britten, C. Brown, S. Herman, B. Golick, M. Kartz, J. Miller, H. T. Powell, M. Vergino and V. Yanovsky, 'Petawatt laser pulses', *Opt. Lett.*, vol. 24(3), p. 160, 1999. (Cited on page 16.)

[49] D. Javorkova, *The CPA System for the PW Peak Intensity at PHELIX*, Ph.D. thesis, Comenius University Bratislava, 2007. (Cited on page 18.)

[50] T. Kühl, D. Ursescu, V. Bagnoud, D. Javorkova, O. Rosmej, K. Cassou, S. Kazamias, A. Klisnick, D. Ros, P. Nickles, B. Zielbauer, J. Dunn, P. Neumayer, G. Pert and the PHELIX team, 'Optimization of the non-normal incidence, transient pumped plasma XRL for laser spectroscopy and plasma diagnostics at FAIR', *Laser and Particle Beams*, vol. 25, p. 93, 2007. (Cited on page 18.)

[51] A. Klisnick, P. Zeitoun, D. Ros, A. Carillon, P. Fourcade, S. Hubert, G. Jamelot, C. L. S. Lewis, A. G. Mac Phee, R. M. N. O'Rourcke, R. Keenan, P. V. Nickles, K. Janulewicz, M. Kalashnikov, J. Warwick, J.-C. Chanteloup, A. Migus, E. Salmon, C. Sauteret and J. P. Zou, 'Transient pumping of a Ni-like Ag x-ray laser with a subpicosecond pump pulse in a traveling-wave irradiation geometry', *JOSA B*, vol. 17, p. 1093, 2000. (Cited on page 20.)

[52] D. Ursescu, *Grazing Incidence Pumped Zr X-Ray Laser for Spectroscopy on Li-like Ions*, Ph.D. thesis, Johannes Gutenberg-Universität Mainz, 2006. (Cited on page 20.)

[53] K. Cassou, S. Kazamias, D. Ros, F. Plé, G. Jamelot, A. Klisnick, O. Lundh, F. Lindau, A. Persson, C.-G. Wahlström, S. de Rossi, D. Joyeux, B. Zielbauer, D. Ursescu and T. Kühl, 'Optimization toward a high-average-brightness soft-x-ray laser pumped at grazing incidence', *Opt. Lett.*, vol. 32(2), p. 139, 2007. (Cited on pages 25 and 28.)

[54] M. Dyba and S. W. Hell, 'Focal Spots of Size lambda /23 Open Up Far-Field Fluorescence Microscopy at 33 nm Axial Resolution', *Phys. Rev. Lett.*, vol. 88(16), p. 163901, 2002. (Cited on page 25.)

[55] S. Kazamias, K. Cassou, D. Ros, F. Plé, G. Jamelot, A. Klisnick, O. Lundh, F. Lindau, A. Persson, C.-G. Wahlström, S. de Rossi, D. Joyeux, B. Zielbauer, D. Ursescu and T. Kühl, 'Characterization of a transient collisional Ni-like molybdenum soft x-ray laser pumped in grazing incidence', *Physical Review A*, submitted 2007. (Cited on pages 27, 28, and 42.)

[56] O. Guilbaud, A. Klisnick, K. Cassou, S. Kazamias, D. Ros, G. Jamelot, D. Joyeux and D. Phalippou, 'Origin of microstructures in picosecond X-ray laser beams', *Europhysics Letters (EPL)*, vol. 74(5), p. 823, 2006. (Cited on pages 28, 42, and 59.)

[57] B. Zielbauer, D. Ursescu, T. Kühl, S. Kazamias, K. Cassou, D. Ros, F. Plé, G. Jamelot, A. Klisnick, O. Lundh, F. Lindau, A. Persson, C.-G. Wahlström, S. de Rossi and D. Joyeux, 'X-Ray Imaging of the Heating Zone of Non-Normal Incidence Pumped XRL Plasma', in 'X-Ray Lasers 2006 Springer proceedings in Physics 115 10th International XRL Conference, Berlin, Germany', , 2006. (Cited on page 29.)

[58] F. Lindau, O. Lundh, A. Persson, K. Cassou, S. Kazamias, D. Ros, F. Plé, G. Jamelot, A. Klisnick, S. de Rossi, D. Joyeux, B. Zielbauer, D. Ursescu, T. Kühl and C.-G. Wahlström, 'Quantitative study of 10 Hz operation of a soft x-ray laser - energy stability and target considerations', *Opt. Express*, vol. 15(15), p. 9486, 2007. (Cited on pages 32 and 33.)

[59] Y. Ochi, N. Hasegawa, T. Kawachi, K. Nagashima, M. Kishimoto, M. Tanaka, M. Nishikino, K. Sukegawa, H. Yamatani and Y. Kunieda, 'Development of 0.1-hz Repetition Driver Laser for the TCE X-Ray Lasers', in 'X-Ray Lasers 2006 Springer proceedings in Physics 115 10th International XRL Conference, Berlin, Germany', , 2006. (Cited on page 34.)

[60] Y. Wang, M. A. Larotonda, B. M. Luther, D. Alessi, M. Berrill, V. N. Shlyaptsev and J. J. Rocca, 'Demonstration of high-repetition-rate tabletop soft-x-ray lasers with saturated output at wavelengths down to 13.9 nm and gain down to 10.9 nm', *Phys. Rev. A*, vol. 72(5), p. 053807, 2005. (Cited on pages 40 and 58.)

[61] M. Tanaka, T. Kawachi, M. Kado, N. Hasegawa, K. Sukegawa, P. Lu, K. Nagashima, Y. Kato and H. Takenaka, 'Near Field Imaging of the Transient Collisional Excitation Ni-like Ag X-ray Laser', *Surface Review and Letters*, vol. 9, p. 641, 2002. (Cited on page 42.)

[62] J. Dunn, R. Keenan and V. N. Shlyaptsev, 'Grazing Incidence Pumping for High Efficiency X-ray Lasers', *Proceedings of SPIE*, vol. 5919, p. 591905, 2005. (Cited on page 44.)

[63] H. Daido, S. Ninomiya, T. Imani, Y. Okaichi, M. Takagi, R. Kodama, H. Takabe, Y. Kato, F. Koike, J. Nilsen and K. Murai, 'Atomic Number Scaling of the Nickel-Like Soft X-Ray Lasers', *International Journal of Modern Physics B [Condensed Matter Physics; Statistical Physics; Applied Physics]*, vol. 11, p. 945, 1997. (Cited on page 46.)

[64] D. F. Zimmer, *Spektroskopische Diagnose eines Röntgenlaserplasmas*, Master's thesis, Universität Mainz, 2007. (Cited on pages 46, 47, and 57.)

[65] LBNL, 'Center for X-Ray Optics', http://www-cxro.lbl.gov/, 2007. (Cited on page 46.)

[66] SPECTRW3, 'online database on spectral properties of atoms and ions', http://spectr-w3.snz.ru, 2007. (Cited on page 46.)

[67] S. Borneis, B. Becker de Moos, H. J. Kluge, T. Kühl, D. Marx, P. Nickles, P. Neumayer, W. Sandner and W. Seelig, 'X-ray laser spectroscopy at the ESR: A proposed novel tool for the investigation of exotic isotopes', *Hyperfine Interactions*, vol. 127(1), p. 537, 2000. (Cited on page 51.)

[68] I. Klaft et al., 'Precision Laser Spectroscopy of the Ground State Hyperfine Splitting of Hydrogenlike $^{209}Bi^{82+}$', *Phys. Rev. Lett.*, vol. 73, p. 2425, 1994. (Cited on page 51.)

[69] P. Seelig et al., 'Ground State Hyperfine Splitting of Hydrogenlike $^{207}Pb^{81+}$ by Laser Excitation of a Bunched Ion Beam in the GSI Experimental Storage Ring', *Phys. Rev. Lett.*, vol. 22, p. 4824, 1998. (Cited on page 51.)

[70] T. Kühl, 'Storage Ring Laser Spectroscopy', *Advances in Atomic, Molecular, and Optical Physics*, vol. 40, p. 113, 1999. (Cited on page 51.)

[71] J. Eberz, U. Dinger, G. Huber, H. Lochmann, R. Menges, R. Neugart, R. Kirchner, O. Klepper, T. Kuhl, D. Marx, G. Ulm and K. Wendt, 'Spins, moments and mean square charge radii of 104-127In determined by laser spectroscopy', *Nuclear Physics A*, vol. 464(1), p. 9, 1987. (Cited on page 51.)

[72] K. D. A. Wendt, 'Feature Article: Laser-Based Ionization Techniques in Rare Isotope Research: Production, Spectroscopy, and Detection', *Nuclear Physics News*, vol. 14(3), p. 1, 2004. (Cited on page 51.)

[73] E. W. Otten, *Treatise on Heavy-Ion Science*, chap. Nuclear Radii and Moments of Unstable Isotopes, p. 517, Plenum Press, New York, 1989. (Cited on page 51.)

[74] Y.-K. Kim, D. H. Baik, P. Indelicato and J. P. Desclaux, 'Resonance transition energies of Li-, Na-, and Cu-like ions', *Phys. Rev. A*, vol. 44, p. 148, 1991. (Cited on page 51.)

[75] T. Beier, L. Dahl, H.-J. Kluge, C. Kozhuharov and W. Quint, 'Trapping ions of hydrogen-like uranium: The HITRAP project at GSI', *Nuclear Instruments and Methods in Physics Research Section B: Beam Interactions with Materials and Atoms*, vol. 235(1-4), p. 473, 2005. (Cited on page 53.)

[76] H. Winter, *Laserspektroskopie an schweren Ionen: Laserinduzierte Zweistufen-Rekombination, Hyperfeinstrukturaufspaltung und g-Faktor des gebundenen Elektrons*, Ph.D. thesis, Technische Universität Darmstadt, 1999. (Cited on page 53.)

[77] S. L. Pape, P. Zeitoun, J. J. Rocca, A. Carillon, P. Dhez, M. Francois, S. Hubert, M. Idir and D. Ros, 'Characterisation of an X-ray laser beam', *SPIE Proceedings*, vol. 4505, p. 23, 2001. (Cited on page 54.)

[78] K. T. Cheng, Y.-K. Kim and J. P. Desclaux, 'Electric Dipole, Quadrupole, and Magnetic Dipole Transition Propabilities of Ions Isoelectronic to the First-Row Atoms, Li through F', *Atomic Data and Nuclear Data Tables*, vol. 24, p. 111, 1979. (Cited on page 54.)

[79] P. Zeitoun, G. Faivre, S. Sebban, T. Mocek, A. Hallou, M. Fajardo, D. Aubert, P. Balcou, F. Burgy, D. Douillet, S. Kazamias, G. de Lachaze-Murel, T. Lefrou, S. le Pape, P. Mercare, H. Merdji, A. S. Morlens, J. P. Rousseau and C. Valentin, 'A high-intensity highly coherent soft X-ray femtosecond laser seeded by a high harmonic beam', *Nature*, vol. 431, p. 426, 2004. (Cited on page 59.)

[80] J. Filevich, J. J. Rocca, M. C. Marconi, R. F. Smith, J. Dunn, R. Keenan, J. R. Hunter, S. J. Moon, J. Nilsen, A. Ng and V. N. Shlyaptsev, 'Picosecond-Resolution Soft-X-Ray Laser Plasma Interferometry', *Appl. Opt.*, vol. 43(19), p. 3938, 2004. (Cited on page 61.)

[81] C. Brewer, F. Brizuela, G. Vaschenko, Y. Wang, M. Larotonda, B. Luther, M. Marconi, J. Rocca, C. Menoni, E. Anderson, W. Chao, Y. Liu and D. Attwood, 'Light-Based Microscopy Reaches Sub-38-nm Resolution with Extreme UV Laser', *Opt. Photon. News*, vol. 17(12), p. 45, 2006. (Cited on page 61.)

[82] S. Kazamias, K. Cassou, D. Ros, F. Plé, G. Jamelot, A. Klisnick, O. Lundh, F. Lindau, A. Persson, C. G. Wahlström, S. de Rossiand D Joyeux, B. Zielbauer and D. Ursescu, 'Laser XUV haute cadence pompé par laser Titane : Saphir, vers la station LASERIX', *Journal de Physique IV*, vol. 138, p. 13, 2007. (Cited on page 61.)